Forside

Eksamensinformation
NFYB05035E - Bachelor Project in Physics, Niels Bohr Institute - Group project

Besvarelsen afleveres af
Jeppe Breum Jacobsen
dvh803@alumni.ku.dk

Karen Rosbjerg Ovesen
cdv343@alumni.ku.dk

Eksamensadministratorer
Eksamensteam, tel 35 33 64 57
eksamen@science.ku.dk

Bedømmere
Kim Lefmann
Eksaminator
lefmann@nbi.ku.dk

Kristine Niss
Censor
kniss@ruc.dk

Besvarelsesinformationer

Tro og love-erklæring: Ja

Magnetic frustration in rare earth garnets

Modelling magnetic interactions in $Gd_3Ga_5O_{12}$ and $Yb_3Ga_5O_{12}$ using Spinteract

Bachelor's thesis

Written by *Karen Rosbjerg Ovesen and Jeppe Breum Jacobsen*

June 16, 2023

Supervised by
Henrik Jacobsen, Kim Lefmann

University of Copenhagen

UNIVERSITY OF COPENHAGEN

Name of Faculty:	SCIENCE
Name of Institute:	Niels Bohr Institute
Author(s):	Karen Rosbjerg Ovesen and Jeppe Breum Jacobsen
Email:	cdv343@alumni.ku.dk, dvh803@alumni.ku.dk
Title and subtitle:	Magnetic frustration in rare earth garnets - Modelling magnetic interactions in $Gd_3Ga_5O_{12}$ and $Yb_3Ga_5O_{12}$ using Spinteract
Supervisor(s):	Henrik Jacobsen, Kim Lefmann
Handed in:	16.06.2023
Defended:	22.06.2023

Abstract

In this thesis, we aim to investigate the magnetic interactions that occur in two magnetically frustrated rare earth garnets. The standard approach for doing this includes performing inelastic neutron scattering on a material below its magnetic ordering temperature and then applying spin wave theory to fit an interaction Hamiltonian to the obtained data. A newly-developed program, Spinteract, uses diffuse scattering data taken above a material's ordering temperature and semiclassical reaction-field theory to do this instead. We use this program to study the magnetic interactions in the rare earth compounds $Gd_3Ga_5O_{12}$ and $Yb_3Ga_5O_{12}$. We verify established exchange interactions for $Gd_3Ga_5O_{12}$ obtaining $J_1 = 130\pm3\,\mathrm{mK}$, $J_2 = -3.9\pm0.1\,\mathrm{mK}$, $J_3 = 4.2 \pm 0.7\,\mathrm{mK}$, $J_4 = 4.0 \pm 0.4\,\mathrm{mK}$ and the theoretical dipolar interaction strength of $\mathcal{D} = 45.7\,\mathrm{mK}$. Then, using Spinteract we fit three Hamiltonians with interaction parameters $\mathcal{D}$, $J_1\mathcal{D}$, and $J_1J_2\mathcal{D}$ respectively to inelastic neutron scattering data taken on $Yb_3Ga_5O_{12}$. We also calculate proposed interaction models found in various literature. We compare these results and find an optimal magnetic Hamiltonian describing $Yb_3Ga_5O_{12}$ to include a dipolar interaction strength of $\mathcal{D} \approx 240\,\mathrm{mK}$ and potentially including a nearest neighbour exchange interaction J_1 in the range $-\mathcal{D}/g_J^2 < J_1 < -25\%\mathcal{D}/g_J^2$, indicative of ferromagnetic interactions, where g_J is the Landé g-factor. The quality of the data makes the quantitative size of the found interaction parameters questionable. However, Spinteract sufficiently replicates the qualitative features of the data building confidence that a $J_1\mathcal{D}$ model is a potentially adequate candidate for describing $Yb_3Ga_5O_{12}$. We also confirm that an anisotropic g-factor is required to describe the data.

Acknowledgements

Writing this thesis over the past four months has been an immensely rewarding journey in many ways. It has been a most fascinating process to understand and analyse the neutron scattering data from these exotic crystals, and we have learned more than we thought possible. The collaboration has brought us closer as friends and for that, we are grateful.

This thesis would not have been possible without the generous support of many people. First and foremost, a huge thanks goes out to our supervisors, Henrik Jacobsen and Kim Lefmann, who have gone above and beyond. They have taught us almost everything we know about magnetism and neutron scattering, and truly made us feel like the work we were doing was important, and always prioritized us. We are grateful for being introduced to their field.

Without the Spinteract program and the neutron scattering data on GGG and YbGG, we could not have made this thesis. Therefore, we would like to thank Joseph A. M. Paddison for creating Spinteract and helping us use it, and Oleg A. Petrenko, Pascalle P. Deen and Lise Ø. Sandberg for allowing us to use their data.

It has been a privilege to work around all the people of the X-ray and Neutron Science group, who have motivated us to push ourselves further. Whether it be at lunch club, in group meetings or around the office, we have always felt welcome.

Contents

1 Introduction

In magnetically frustrated systems, competing interactions prohibit the system from ordering into one unique ground state. Instead, many different states minimizing the energy become available. The spins of the system remain disordered but may still be correlated resulting in the emergence of novel states of matter [12]. Magnetic frustration appears in some systems with rare earth ions like the two isostructural compounds gadolinium gallium garnet $Gd_3Ga_5O_{12}$ (GGG) and ytterbium gallium garnet $Yb_3Ga_5O_{12}$ (YbGG) studied in this report. In these examples, frustration appears due to competing spin-spin interactions and anisotropy.

A variety of methods have been used to investigate the emergent magnetic behaviour in these systems [6, 10, 11, 12]. Unlike previous methods, which relied on more specialized solutions to specific problems, a newly developed program, Spinteract [9], promises to fit interaction parameters directly to experimental data from neutron scattering experiments taken above a material's ordering temperature.

In this thesis, we use the program to investigate the magnetic interactions of GGG, which have already been studied using Spinteract by Joe Paddison, its creator, in order to benchmark the program, and then we use it on the less-studied YbGG. First, we recreate Paddison's results for GGG to gain knowledge of and practice in using the program. Moving on to YbGG, we start by fitting various interaction parameters to our neutron scattering data to find Spinteract's own optimal model for the material and then, we use the program to generate other proposed models found in various literature [8, 11]. Ultimately, the aim of this report is to explore and display Spinteract's ability to generate and compare various magnetic Hamiltonians, and to gain knowledge of the magnetic interactions that govern the mysterious YbGG.

2 Magnetism and frustration

In this chapter, we provide the necessary theoretical foundation to understand the relevant magnetic interactions for the two materials studied in this report. We start by introducing some basic concepts in magnetism followed by a description of the magnetic Hamiltonian we use to fit our data. Then to gain insight into magnetic excitations, we introduce spin wave theory by deriving the dispersion relation of a one-dimensional ferromagnetic spin chain. Finally, we make a short outline of magnetic frustration focusing on how the phenomenon appears in the garnet structure. The following sections are mainly based on ref. [1].

2.1 Magnetic moments

This report studies the magnetic properties of two rare earth garnets, $Gd_3Ga_5O_{12}$ (GGG) and $Yb_3Ga_5O_{12}$ (YbGG). Rare earth garnets are a type of crystal which takes the form $A_3B_5O_{12}$. Here, A is the rare earth ion, for our purpose Gd^{3+} or Yb^{3+}, B is a non-magnetic ion, and O is oxygen. Both GGG and YbGG have gallium (Ga) as their non-magnetic ion [3]. In rare earth ions, electrons in the 4f orbitals carry the magnetic moment, $\boldsymbol{\mu}$, which is described by

$$\boldsymbol{\mu} = \mu_B(g_L\mathbf{L} + g_S\mathbf{S}) = \mu_B g\mathbf{J}. \tag{2.1}$$

Here, μ_B is the Bohr magneton, $\mathbf{L}$ is the orbital angular momentum of the ion with g-factor g_L,

S is the spin angular momentum of the ion with g-factor g_S, **J** is the total angular momentum, and g is the g-factor. One estimate of the g-factor is the Landé g-factor:

$$g_J = \frac{3}{2} + \frac{S(S+1) - L(L+1)}{2J(J+1)}. \tag{2.2}$$

The RHS of eq. (2.1) is favorable to use when **L** and **S** are not separately conserved which is generally the case for rare earth ions. This is true for Yb^{3+} but not for Gd^{3+}. This definition makes the assumption that $g_L = 1$ and $g_s = 2$. In general, the g-factor is a tensor which is assumed to be isotropic in eq. (2.2) but in eq. (2.1), g has to be treated as a matrix.

2.2 Hund's rules

In their ionic state, both Gd and Yb have unfilled 4f shells. Gd^{3+} has the electron configuration $[Xe]4f^7$, and Yb^{3+} has $[Xe]4f^{13}$. To figure out how the electrons fill these shells, we apply Hund's rules. Hund's rules can be used to estimate the combination of quantum numbers which minimizes the energy of the atom. It is important to note that these rules, which can only give information about the ground state configuration, serve as guidelines and ignore crystal field effects which can be significant in some cases [1]. The rules can be summarized as follows:

(1) Maximize S. The Pauli exclusion principle prohibits electrons of equal spin from being in the same place. This spreads out the electrons resulting in a lower Coulomb energy.

(2) Maximize L. If we put the electrons in orbits rotating the same way around the nucleus, the average distance between them will be larger, once again resulting in the lowest possible Coulomb energy.

(3) $J = |L \pm S|$. Positive sign if the shell is more than half full, and negative sign for a shell less than half full. This rule is only applicable if spin-orbit coupling plays a significant role in the energy of the state, which is the case for rare earth ions.

Applying these rules to Gd^{3+}, we note that $\ell = 3$ for an f shell. To satisfy the first rule, we put $2\ell + 1 = 7$ electrons in the spin-up state. Since Gd^{3+} only has 7 electrons in the f-shell, we are done, and $S = +\frac{1}{2} \cdot 7 = \frac{7}{2}$, $L = 0$, and $J = \frac{7}{2}$.

For Yb^{3+}, we fill $2\ell + 1 = 7$ electrons in the spin-up state. Satisfying the second rule, we fill the remaining 6 electrons in the spin-down state, starting from $m_l = 3$ down to $m_l = -2$. Now, $S = +\frac{1}{2} \cdot 7 - \frac{1}{2} \cdot 6 = \frac{1}{2}$, $L = 3$, and $J = |L + S| = \frac{7}{2}$. This is summarized in table 1.

↑↓ \ m_l	3	2	1	0	-1	-2	-3
↑	x	x	x	x	x	x	x
↓							

↑↓ \ m_l	3	2	1	0	-1	-2	-3
↑	x	x	x	x	x	x	x
↓	x	x	x	x	x	x	

Table 1: Hund's rules applied to the $4f^7$ electrons of Gd^{3+} (Left) and the $4f^{13}$ electrons of Yb^{3+} (Right).

While Hund's rules work for Gd^{3+}, this is not always the case for Yb^{3+}. The ground state of the Yb^{3+} ion is called a Kramer's doublet and is an effective spin-$\frac{1}{2}$ where $m_j = \pm\frac{7}{2}$ [11]. Due to strong crystal field effects in YbGG, the g-factor is slightly anisotropic, and one needs to use

a g-tensor in eq. (2.1). The diagonal elements of this tensor have previously been found to be $g = (2.84, 3.59, -3.72)$ in local coordinates [8] while all off-diagonal elements are 0. For GGG, the Landé g-factor $g_J = 2$ obtained from eq. (2.2) is used.

2.3 The magnetic Hamiltonian

This report includes two contributions to the spin Hamiltonian of GGG and YbGG to describe their magnetic properties: The (direct) exchange interaction, $\mathcal{H}_{ex}$, and the dipole interaction, $\mathcal{H}_{dip}$, resulting in the following Hamiltonian:

$$\mathcal{H} = \mathcal{H}_{ex} + \mathcal{H}_{dip}. \tag{2.3}$$

2.3.1 The exchange interaction

The exchange interaction arises from the Pauli exclusion principle and electrostatic interactions as particles of the same charge save energy when they are further apart due to the repulsive Coulomb force. This is equivalent to satisfying Hund's first rule.

The exchange term in 2.3 can be expressed by the Heisenberg Hamiltonian which includes the interaction between all ion sites in the system and with spins free to point in all directions:

$$\mathcal{H}_{ex} = \sum_{i,j} J_{i,j} \mathbf{S}_i \cdot \mathbf{S}_j. \tag{2.4}$$

Here, $\mathbf{S}_i$ and $\mathbf{S}_j$ are the total spin angular momenta for the ions at site i and j respectively, and $J_{i,j}$ is the exchange interaction parameter describing the strength of the interaction between spin i and j. The sign of $J_{i,j}$ in eq. (2.4) dictates whether the system is a ferromagnet or an antiferromagnet. If $J_{i,j} < 0$, the system will be in its lowest energy state when the atoms' spin align. This makes it a ferromagnet. If $J_{i,j} > 0$, the spins will want to anti-align to minimize the energy, which in turn makes it an antiferromagnet. Another case in which $J_{i,j} > 0$ is the ferrimagnet where the system consists of multiple sublattices aligned in different directions.

Ferro-, ferri- and antiferromagnetism are three examples of ordered magnetic structures. Magnetic order refers to the ordered sorting of magnetic spins in reference to the crystal lattice of the system. This is a spontaneous phenomenon which appears at different temperatures for different systems [1]. This ordering temperature, T_O, has different names depending on the magnetic order of your system. For ferromagnets, it is called the Curie-Weiss temperature, T_C, while for antiferromagnets, it is called T_N for Néel. In general, ferromagnets at temperatures above T_C and antiferromagnets above T_N will enter a paramagnetic state. In the paramagnetic state, thermal fluctuations are much stronger than interactions between spins and as the temperature rises further, the spins begin to become uncorrelated and will align with an external magnetic field [12].

2.3.2 The dipole interaction

The dipole term, $\mathcal{H}_{dip}$, describes the interaction of magnetic dipole pairs in a material. The interaction between the magnetic moments of two particles, $\boldsymbol{\mu}_i$ and $\boldsymbol{\mu}_j$, contribute an energy to the Hamiltonian. If we include all such dipole pairs, we get the following Hamiltonian:

$$\mathcal{H}_{dip} = \frac{\mu_0}{4\pi} \sum_{i,j} \frac{1}{r_{i,j}^3} \left[\boldsymbol{\mu}_i \cdot \boldsymbol{\mu}_j - \frac{3}{r_{i,j}^2} (\boldsymbol{\mu}_i \cdot \mathbf{r}_{i,j})(\boldsymbol{\mu}_j \cdot \ \mathbf{r}_{i,j}) \right]. \tag{2.5}$$

The dipole interaction acts over long ranges although to quantify it, it is common to denote it by its strength between nearest neighbours. If we only consider the nearest neighbour terms in the sum from eq. (2.5) and use the definition in eq. (2.1), we can pull out the constant

$$D_{Dip} = \frac{\mu_0 \mu_B^2}{4\pi k_B r_{nn}^3}. \tag{2.6}$$

This constant is often expressed in units of temperature, hence we have added a factor of $1/k_B$, where k_B is Boltzmann's constant. r_{nn} is the distance between neighbouring magnetic moments. Not everyone follows the convention put forth in eq. (2.6). Some use $g_L^2 D_{Dip}$ or $|J|^2 g_L^2 D_{Dip}$. In literature, it is common to use the former when describing GGG [6, 9, 10] and the latter when describing YbGG [8, 11]. This is summarized in table 2. In this thesis, we will follow the conventions used in the literature. As such, the dipole interaction parameter will be defined as $\mathcal{D} = g_L^2 D_{Dip}$ for GGG and $\mathcal{D} = |J|^2 g_L^2 D_{Dip}$ for YbGG. For both materials, the squared length of their total angular momentum, $|J|^2 = J(J+1)$, is also included in the exchange parameter $J_{i,j}$. In table 2, we have calculated the theoretical dipole interaction parameters using eq. (2.6) in the different conventions.

Ion	D_{Dip} (mK)	$g_L^2 D_{Dip}$ (mK)	$\lvert J\rvert^2 g_L^2 D_{Dip}$ (mK)
Yb^{3+}	11.94	15.594	245.6
Gd^{3+}	11.52	46.10	726.0

Table 2: Dipole interaction parameters for GGG and YbGG. These values are purely theoretical and calculated using eq. (2.6).

2.4 Spin waves

A well-suited theory for describing magnetic excitations is spin wave theory. As a simple example, we consider a ferromagnet at 0 K. Here, all spins are aligned but at non-zero temperature, excitations are introduced in the form of spin waves. Spin waves can be produced with arbitrarily small energies and are therefore the ferromagnetic analogues to acoustic phonons, the quantum mechanical particle responsible for thermal excitations in solids. The equivalent quasiparticle to the spin wave is the magnon. However, we will stick to the semiclassical wave picture. The spin wave propagates as small precessions in the individual spins as seen in fig. 1. A full derivation of the dispersion relation for spin waves in a one-dimensional (1D) ferromagnetic chain can be found in appendix A but here, we will simply outline the results [1, 14].

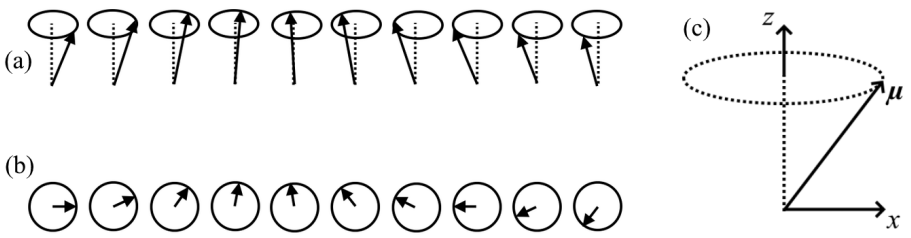

Figure 1: Spins in a 1D ferromagnet form a spin wave at non-zero temperature. (a) Spin wave seen from the side. (b) seen from above. (c) The precession of one spin seen from the side. Adapted from [1]

We use a Heisenberg Hamiltonian that only considers nearest neighbour interactions to describe the system[1]:

$$\hat{\mathcal{H}} = -2J \sum_{\langle i,j \rangle} \hat{\mathbf{S}}_i \cdot \hat{\mathbf{S}}_j. \tag{2.7}$$

Using the Heisenberg equations of motion for any operator $\hat{Q}$ [5],

$$i\hbar \frac{d\hat{Q}}{dt} = [\hat{Q}, \hat{\mathcal{H}}], \tag{2.8}$$

and the commutator relation,

$$[S^x, S^y] = i\hbar \varepsilon_{xyz} S^z, \tag{2.9}$$

to calculate the motion of a spin $\hat{\mathbf{S}}_p = (S_p^x, S_p^y, S_p^z)$ in the chain, we find the relation,

$$\hbar \frac{d\hat{\mathbf{S}}_p}{dt} = 2J\hat{\mathbf{S}}_p \times (\hat{\mathbf{S}}_{p-1} + \hat{\mathbf{S}}_{p+1}). \tag{2.10}$$

Assuming the spins are aligned along the z-direction in the ground state and treating the other spin-components as perturbations produced by excitations, we find a plane wave solution to the spin components. This process yields the dispersion relation

$$\hbar\omega = 4JS(1 - \cos(qa)), \tag{2.11}$$

where S is the spin length, q is the magnitude of the spin wave's wave vector, and a is the spacing between spins. Since this is a continuous function that goes through (0, 0), we can see that spin waves can be created with arbitrarily small energies in a 1D ferromagnet. The dispersion relation can be seen in fig. 2 [1]. It is possible to make similar calculations for more complex systems but only if they have a well-defined ground state.

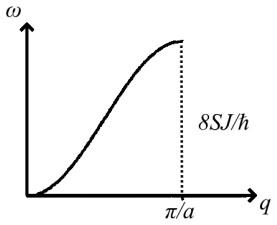

Figure 2: Dispersion relation for a 1D ferromagnetic spin chain from eq. (2.11). Figure from [1]

2.5 Magnetic frustration

In some systems, conflicting interactions make it impossible to find a single ground state. Instead, a variety of similar degenerate ground states minimizes the energy of the system creating a ground state manifold, and the system is said to be frustrated. An example of this is antiferromagnetic (AFM) Ising spins on a triangular lattice as shown in fig. 3 where the system is unable to satisfy competing nearest neighbour interactions and obey anisotropy and lattice geometry at the same time. The two adjacent spins at the bottom of the triangle are able to remain unaligned while the third spin at the top can point either way but will in neither case minimize the energy of both neighbours.

[1] This Hamiltonian uses a different sign than the one in eq. (2.4), the two should not be confused.

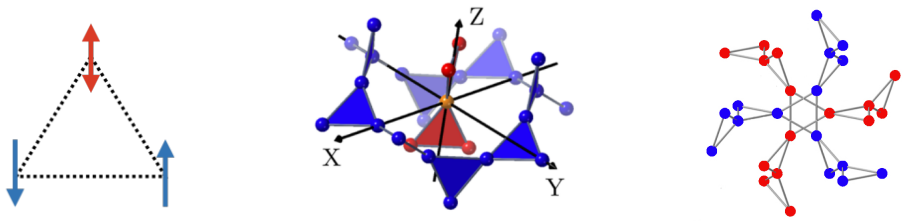

Figure 3: Left: Frustrated antiferromagnetic Ising spins on a triangle. Middle: The hyperkagome lattice with corner sharing triangles, figure from [12]. Right: Two interpenetrating sublattices that make up the hyperkagome lattice, adapted from [3].

Similarly, frustration occurs on a much larger scale for the rare earth compounds studied in this report due to their triangular lattice. GGG and YbGG belong to space group $Ia\bar{3}d$ with their magnetic ion of interest at Wyckoff position 24c. These ions lie on two interpenetrating sublattices, each with corner sharing triangles [10], as seen on the right in fig. 3. The angle between the planes spanning two such neighbouring triangles is 73.2°. This is known as a hyperkagome lattice [3]. This structure is illustrated in the middle on fig. 3. The space group and Wyckoff position together with characteristic lengths allow a computer program to calculate the coordinates of all the magnetic ions for simulation.

For frustrated systems such as those considered here, it is not possible to model excitations with spin wave theory since they do not have well-defined ground states.

3 Neutron scattering

Neutron scattering is a popular technique for investigating the atomic and magnetic structure and dynamics of various materials. In the following sections, which are mainly based on [14] and [7], we outline the fundamental principles and important equations in neutron scattering.

3.1 Fundamentals of neutron scattering

Neutrons carry no electric charge which allows them to probe the bulk of materials and scatter from nuclei through the strong nuclear force rather than scattering at the surface. Additionally, neutrons posses a magnetic moment which also allows them to scatter due to magnetic interactions. These facts are exactly what the neutron scattering technique takes advantage of as this can be used to investigate the atomic and magnetic structure in a given sample. The magnetic moment of a neutron is

$$\mu_n = \gamma\mu_N = -9.6624 \times 10^{-27}\,\mathrm{JT}^{-1}, \tag{3.1}$$

where γ is the gyromagnetic ratio of the neutron, and μ_N is the nuclear magneton. In a neutron scattering experiment, high energy (MeV) neutrons are produced, often as by-products from fission or from particle accelerators. The high energy neutrons are slowed down, moderated, to have energies in the meV range before entering a neutron guide which directs them toward a sample. After scattering from the sample, the neutrons are measured by a detector [7].

3.2 Geometry of solids

To understand the derivation of various neutron scattering equations in the following sections as well as single crystal scattering profiles introduced in later chapters, some understanding of the geometry of solids is required. This section only presents what is necessary for this thesis. For a deeper understanding we refer to [14], upon which this section is based.

In some materials, the atoms arrange themselves in a periodic structure known as a lattice. A lattice is made up of an infinite set of points given by lattice vectors $\mathbf{R}_{n_1,n_2,n_3} = n_1\mathbf{a}_1 + n_2\mathbf{a}_2 + n_3\mathbf{a}_3$, $n_i \in \mathbb{Z}$, where $\mathbf{a}_i$ are linearly independent lattice vectors. Given these lattice points, we define the primitive unit cell as the space containing one lattice point which, when repeated, creates the complete lattice. We define the density of lattice points as

$$\rho(\mathbf{r}) = \sum_{n_{1,2,3}} \delta(\mathbf{r} - \mathbf{R}_{n_1,n_2,n_3}), \tag{3.2}$$

where δ is the delta function, and $\mathbf{r}$ is some point in space. This density is periodic in $\mathbf{R}$ meaning $\rho(\mathbf{r}) = \rho(\mathbf{r} + \mathbf{R})$ for any $\mathbf{R}$. It turns out that a lattice defined in terms of so-called reciprocal lattice vectors is very useful. To construct the reciprocal lattice, we wish to create a set of plane waves with the same periodicity as $\rho(\mathbf{r})$, i.e. a Fourier transform. The wave vectors of the plane waves will be made up of the reciprocal lattice vectors, which we will denote $\mathbf{b}_i$. A point in reciprocal space will then be $\mathbf{G}_{m_1,m_2,m_3} = m_1\mathbf{b}_1 + m_2\mathbf{b}_2 + m_3\mathbf{b}_3$, $m_i \in \mathbb{Z}$. Now, we take the Fourier transform of the density and invoke the periodicity in $\mathbf{R}$:

$$\mathcal{F}(\rho(\mathbf{r})) = \sum_{n_{1,2,3}} e^{i\mathbf{G}\cdot\mathbf{r}} \tag{3.3}$$

$$= \sum_{n_{1,2,3}} e^{i\mathbf{G}\cdot(\mathbf{r}+\mathbf{R})} \Rightarrow e^{i\mathbf{G}\cdot\mathbf{R}} = 1, \tag{3.4}$$

which implies that

$$\mathbf{a}_i \cdot \mathbf{b}_j = 2\pi\delta_{ij}, \tag{3.5}$$

where δ_{ij} is the Kronecker delta. To better understand the reciprocal lattice, we look at lattice planes. A family of lattice planes is an infinite set of planes that contains all lattice points, and where the planes are equally separated and parallel. We specify the different families of planes in terms of Miller indices. In our two-dimensional (2D) example on fig. 4, the lattice lines are separated by $1\mathbf{a}_2$ in the $\hat{\mathbf{a}}_2$-direction. In the $\hat{\mathbf{a}}_1$-direction, we say that they are separated by an infinite number of $\mathbf{a}_1$-vectors. We define the Miller indices as the reciprocal values of these separations, so the Miller indices of the lattice lines in fig. 4 are (01). Then, the reciprocal lattice vector given by $0\mathbf{b}_1 + 1\mathbf{b}_2$ will be a normal vector to the lattice lines. For a three-dimensional (3D) lattice, we simply invoke eq. (3.5) once more when constructing the reciprocal lattice.

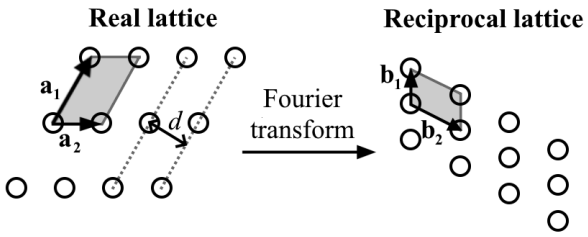

Figure 4: Left: 2D crystal lattice in real space with lattice vectors $\mathbf{a}_1$ and $\mathbf{a}_2$. The shaded area is a primitive unit cell. The dotted lines show two lattice lines. Right: The corresponding primitive reciprocal lattice obtained from a Fourier transform with reciprocal lattice vectors $\mathbf{b}_1$ and $\mathbf{b}_2$.

In 3D, we call the Miller indices (hkl) and define the reciprocal lattice vector $\mathbf{G}_{hkl} = h\mathbf{b}_1 + k\mathbf{b}_2 + l\mathbf{b}_3$. It is common to define directions in a lattice in terms of the corresponding reciprocal lattice vector (hkl). For negative Miller indices, an over-bar is used instead of a minus sign.

3.3 Elastic neutron scattering

In elastic neutron scattering, the neutrons do not exchange energy with the sample and hence, their initial wave vector, $\mathbf{k}$, is equal in magnitude to the final wave vector, $\mathbf{k}'$:

$$|\mathbf{k}| = |\mathbf{k}'|. \tag{3.6}$$

By using Fermi's golden rule, one can determine how many neutrons scatter and where. Fermi's golden rule gives us the transition rate per unit time, $\Gamma(\mathbf{k}', \mathbf{k})$, from $\mathbf{k}$ to $\mathbf{k}'$. If we simply imagine the sample as a potential, $V(\mathbf{r})$, that the neutrons interact with, we can relate it to the transition rate via $\Gamma(\mathbf{k}', \mathbf{k}) \propto \langle \mathbf{k}' | V(\mathbf{r}) | \mathbf{k} \rangle^2$. Additionally, we assume the wave functions of the neutrons to be time-independent, so the matrix element becomes

$$\langle \mathbf{k}' | V(\mathbf{r}) | \mathbf{k} \rangle = \frac{1}{L^3} \int \mathbf{dr}\, e^{-i(\mathbf{k}'-\mathbf{k})\cdot\mathbf{r}} V(\mathbf{r}). \tag{3.7}$$

Since we are working with a crystal, we only integrate over points in a single unit cell, $\mathbf{x}$, and sum over all of them.

$$\langle \mathbf{k}' | V(\mathbf{r}) | \mathbf{k} \rangle = \frac{1}{L^3} \sum_{\mathbf{R}} \int_{unit\ cell} \mathbf{dx}\, e^{-i(\mathbf{k}'-\mathbf{k})\cdot(\mathbf{x}+\mathbf{R})} V(\mathbf{x}+\mathbf{R}) \tag{3.8}$$

$$= \frac{1}{L^3} \left[\sum_{\mathbf{R}} e^{-i(\mathbf{k}'-\mathbf{k})\cdot\mathbf{R}} \right] \left[\int_{unit\ cell} \mathbf{dx}\, e^{-i(\mathbf{k}'-\mathbf{k})\cdot\mathbf{x}} V(\mathbf{x}) \right], \tag{3.9}$$

where we use the fact that $V(\mathbf{x}+\mathbf{R}) = V(\mathbf{x})$ because of the periodicity of the crystal. If $\mathbf{k}' - \mathbf{k} \neq \mathbf{G}$, each $\mathbf{R}$ in the sum will contribute with a point on the complex unit circle and as the number of unit cells increases, the sum will approach 0. However if $\mathbf{k}' - \mathbf{k} = \mathbf{G}$, each term is equal to 1. This is known as the Laue condition, which is equivalent to Bragg's law:

$$\frac{|\mathbf{G}|}{2} = |\mathbf{k}| \sin\theta \qquad \Rightarrow \qquad |\mathbf{G}| = \frac{4\pi}{\lambda} \sin\theta \tag{3.10}$$

The geometry of this derivation can be seen in fig. 5 (a). Here, λ is the (de Broglie) wavelength of the neutron, and θ is the scattering angle.

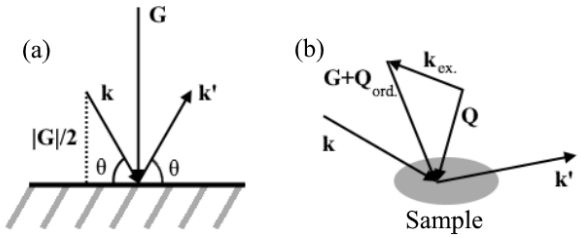

Figure 5: Geometry of scattering in reciprocal space. (a) Elastic scattering, the geometry implies that $|\mathbf{G}|/2 = |\mathbf{k}| \sin\theta$. (b) Inelastic scattering, conservation of momentum requires that $\mathbf{Q} = \mathbf{G} + \mathbf{Q}_{ord.} + \mathbf{k}_{ex.}$.

The integral in eq. (3.9) is called the structure factor, $F(\mathbf{Q})$, where $\mathbf{Q} = \mathbf{k} - \mathbf{k}'$ is the scattering vector. As an example of a potential, let us consider the Fermi pseudo-potential which is a delta function at each atomic site j,

$$V(\mathbf{x}) = \frac{2\pi\hbar^2}{m_n} \sum_j b_j \delta(\mathbf{x} - \mathbf{x}_j). \tag{3.11}$$

b_j is known as the scattering length and is a measure of "how strong" the neutrons scatter from nucleus j. This potential is a good approximation of the strong nuclear interaction between neutrons and nuclei. We can insert this potential in the structure factor resulting in

$$F_N(\mathbf{Q}) = \frac{2\pi\hbar^2}{m_n} \sum_j b_j \int_{unit\ cell} \mathbf{dx}\, \mathrm{e}^{i\mathbf{Q}\cdot\mathbf{x}} \delta(\mathbf{x} - \mathbf{x}_j) \tag{3.12}$$

$$= \frac{2\pi\hbar^2}{m_n} \sum_j b_j \mathrm{e}^{i\mathbf{Q}\cdot\mathbf{x}_j}. \tag{3.13}$$

We add the subscript N to indicate that this is the nuclear structure factor. Intensities measured in experiments are proportional to $\Gamma(\mathbf{k}', \mathbf{k})$, which in turn is proportional to the structure factor. In section 3.2, we discussed how Miller indices define lattice planes and thus, we find

$$I_{hkl} \propto |F_{hkl}|^2. \tag{3.14}$$

This means that the scattering intensity off the lattice planes with normal vector $\mathbf{G}_{hkl} = h\mathbf{b}_1 + k\mathbf{b}_2 + l\mathbf{b}_3$ is proportional to the absolute square of the structure factor. A slightly more accurate equation is the master equation of neutron diffraction:

$$\frac{d\sigma}{d\Omega}\Big|_{coh.\ nuc.} = \mathrm{e}^{-2W} \frac{N(2\pi)^3}{V_0} |F_N(\mathbf{Q})|^2 \sum_{\mathbf{G}} \delta(\mathbf{Q} - \mathbf{G}), \tag{3.15}$$

where σ is the scattering cross section defined as the number of neutrons scattered per second divided by the neutron flux corresponding to an effective area. $d\sigma$ is an element of this effective area, and $d\Omega$ is a solid angle element. e^{-2W} is the Debye-Waller factor which describes the fact that some neutrons scatter from phonons. N is the number of unit cells with volume V_0. The LHS is known as the differential scattering cross section and is proportional to the probability of a neutron scattering into $d\Omega$. The subscript *coh. nuc.* refers to the fact that the scattering happens because of our periodic nuclear potential and not from random events.

A derivation of the analogous equation for magnetic scattering is outside the scope of this thesis. Instead, the elastic magnetic diffraction cross section from [7] is presented here:

$$\frac{d\sigma}{d\Omega}\Big|_{coh.\ mag.} = (\gamma r_0)^2 \left[\frac{g}{2}F_m(Q)\right]^2 \mathrm{e}^{-2W} \frac{N(2\pi)^3}{V_m}|F_M(\mathbf{Q})|^2 \sum_{\mathbf{G}} \delta(\mathbf{Q}-\mathbf{G}-\mathbf{Q}_{order}), \tag{3.16}$$

where r_0 is the electron radius, and $F_m(Q)$ is the magnetic form factor. N is the number of magnetic unit cells, and V_m is the volume of these. $\mathbf{Q}_{order}$ is the reciprocal lattice vector which minimizes the energy of (i.e. orders) the system, and can be thought of as the magnetic analogous to $\mathbf{G}$. For the dispersion relation found in eq. (2.11) for the 1D ferromagnetic chain, this would correspond to $Q_{order} = 0$. Finally, $F_M(\mathbf{Q})$ is the magnetic structure factor at scattering vector $\mathbf{Q}$. The delta function on the RHS ensures conservation of momentum.

3.4 Inelastic neutron scattering

By measuring the change in the energy of a scattered neutron, one can study the dynamics of a material. Neutrons can disperse or absorb energy when scattering in a material giving rise to excitations. This thesis will only consider magnetic excitations. Energy and momentum conservation imply

$$\hbar\omega = E - E' \qquad\qquad \mathbf{k} = \mathbf{k}' + \mathbf{Q}_{order} + \mathbf{G} + \mathbf{k}_{ex.}, \tag{3.17}$$

such that $\hbar\omega$ is an excitation produced in the sample, and $\mathbf{k}_{ex}$ is the wave vector of the produced excitation. The geometry of inelastic scattering is visualized in fig. 5 (b). The master equation for the partial differential magnetic scattering cross section for unpolarized neutrons is

$$\frac{d^2\sigma}{d\Omega dE'}\Big|_{coh.\ mag.} = (\gamma r_0)^2 \frac{k'}{k} \left[\frac{g}{2}F(Q)\right]^2 \mathrm{e}^{-2W} \sum_{\alpha,\beta} (\delta_{\alpha,\beta} - \hat{\mathbf{Q}}_\alpha \hat{\mathbf{Q}}_\beta) S^{\alpha,\beta}(\mathbf{Q},\omega). \tag{3.18}$$

The LHS is the intensity of neutrons scattered into a solid angle element, $d\Omega$, with infinitesimal energy dE'. α and β run over x, y, z, and the factor $(\delta_{\alpha,\beta} - \hat{\mathbf{Q}}_\alpha \hat{\mathbf{Q}}_\beta)$ ensures that scattering only occurs from perpendicular spin components. The most important factor, $S^{\alpha,\beta}(\mathbf{Q},\omega)$, is the dynamic correlation function:

$$S^{\alpha,\beta}(\mathbf{Q},\omega) = \frac{1}{2\pi\hbar}\int_{-\infty}^{\infty} \sum_{j,j'} \mathrm{e}^{i\mathbf{Q}\cdot(r_{j'}-r_j)} \langle s_j^\alpha(0) s_{j'}^\beta(t)\rangle \mathrm{e}^{-i\omega t}\, dt. \tag{3.19}$$

Here, j and j' run over the spins at positions r_j and $r_{j'}$ with α and β components s^α and s^β. Like the structure factor from eq. (3.13), which was essentially a spatial Fourier transform of the potential, eq. (3.18) is both a spatial and temporal Fourier transform of the correlation between spins in the sample. In experiments, $d^2\sigma/(d\Omega dE')$ is measured, and $S^{\alpha,\beta}(\mathbf{Q},\omega)$ is calculated from a Hamiltonian. These quantities can then be compared, and the parameters of the Hamiltonian can be optimized.

4 Spinteract

In this thesis, we use the program Spinteract, released in October 2022, to model neutron scattering data taken on two different materials. The program has already been used to model magnetic interactions in one of these materials, GGG, and we wish to replicate these results to

develop our understanding of and skills in using the program. Secondly, we use it on the less studied material YbGG. A comprehensive explanation of how Spinteract works, and what sets it apart from alternative methods is outside the scope of this thesis. For more details, see [9]. However, this section should serve as context and motivation for using the program.

A common approach for determining magnetic interactions involves the use of spin wave theory and inelastic neutron scattering performed below a material's ordering temperature, T_O. Some disadvantages of this approach are that the ordered state has to be well-understood as well as reachable within temperatures that are accessible in experiments. In this light, some advantages of using scattering data taken above a material's ordering temperature immediately become apparent. To analyse diffuse scattering data, typically taken above a material's T_O, reverse Monte Carlo methods are often used. However, such methods only describe spin correlations and not the underlying magnetic interactions.

With Spinteract, the user supplies diffuse scattering data from a powder or single-crystal experiment as well as a magnetic Hamiltonian, which includes the relevant interaction parameters of the material. Next, the program calculates its own magnetic scattering intensities based on this model and fits the interaction parameters until a minimal chi-square between experimental data and calculated intensity is obtained.

Spinteract uses a mean-field approach known as Onsager reaction-field theory. The reaction-field method is semiclassical which means that it might not be qualified to describe correlated quantum systems with effective spin-$\frac{1}{2}$, such as YbGG. The long range dipole interaction is implemented with Ewald summation [9].

In Spinteract, inelastic data has to be energy-integrated, essentially losing the energy-dependence. Instead of relying on information about energy tranfers, Spinteract is highly dependent on the specified sample temperature.

To run a refinement in Spinteract, a minimum of three files is needed, all in a .txt-format: One (or more) file(s) containing the diffuse scattering data one wishes to fit to, one configuration file containing crystallographic and magnetic information about the material and finally, one parameter file containing the parameter names and their initial values. The user also specifies the number of points to include in the first Brillouin zone, BZ-points. This is essentially a measure of the resolution used in the fit.

5 Gadolinium Gallium Garnet

In this chapter, data analysis and Spinteract refinements of neutron scattering data taken on $Gd_3Ga_5O_{12}$ (GGG) will be presented and discussed. We use Spinteract to find the optimal model for the well-studied magnetic interactions in GGG and recreate Joe Paddison's results using the same data. As mentioned in 2.3.2, the convention used for GGG will be one where $\mathcal{D} = g_J^2 D_{Dip}$.

5.1 Introduction to GGG

Our powder data on GGG was provided by Joe Paddison, though it was originally produced by Oleg A. Petrenko and his team and published in [10]. The measurements were taken on the D1B instrument at ILL in Grenoble. The data consists of intensity measurements of scattered neutrons as a function of the scattering angle at 18 temperatures ranging from $0.043 - 9\,\mathrm{K}$.

In GGG, the spins partially freeze at $T_f \approx 175\,\text{mK}$ [6]. This is not the same as a long range ordering temperature, but it does indicate a spin glass transition which is associated with a type of ordering [13]. For this reason, only measurements taken above T_f will be considered. Data taken at 9 K is used as a measurement of background scattering under the assumption that we are in the paramagnetic regime where the spins are almost entirely uncorrelated. The 9 K data will be subtracted from the other data sets. Nuclear Bragg peaks are removed prior to any refinements. This treatment of the data can be seen in fig. 6. Uncertainties are only available for the data points used in [9] and thus, this thesis has to use the same points. For this reason, the purpose now is mainly to replicate the results in [9]. The selection of data made in [9] seems reasonable since 0.175 K is the lowest temperature above (or at) T_f. Furthermore, not using data taken above T = 1.04 K seems like an appropriate choice as it is the highest temperature where the small hump at $Q \approx 1.8\,\text{Å}^{-1}$ remains visible in the data. This can be seen on fig. 6.

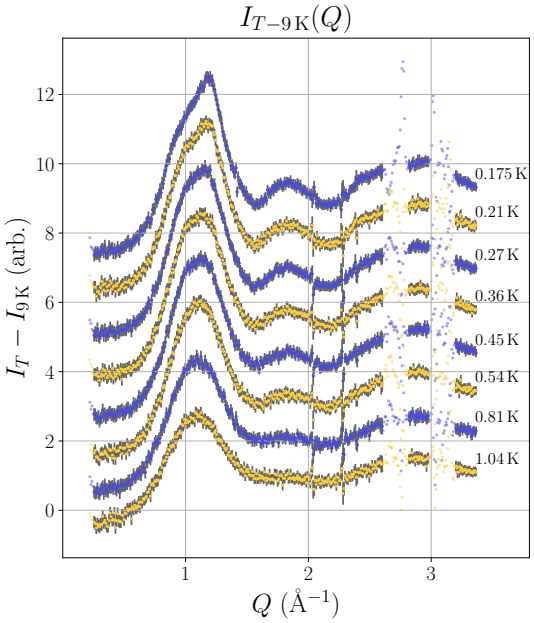

Figure 6: Neutron diffraction data from [10], $I_{T-9\,\text{K}}(Q)$, for GGG between 0.175 - 1.04 K with grey uncertainties. 9 K data subtracted. An arbitrary spacing of 1.2 is added between each curve for clarity. Nuclear Bragg peaks have been removed in the two gaps near $Q \approx 3\,\text{Å}^{-1}$.

5.2 Spinteract refinements of different models

We fit our data to a model described by the Hamiltonian in eq. (2.3) using Spinteract. Initially, only dipole interactions as well as exchange interactions between nearest neighbours are modelled, we will call this a $J_1\mathcal{D}$ model. If this model proves insufficient, next nearest neighbours will be included in a $J_{1-2}\mathcal{D}$ model. This process of considering exchange interactions from further neighbours continues until a satisfactory fit is obtained. A model which considers one more neighbour than the previous one should show improvement in the χ^2_{red} as well as significant qualitative improvements in the shape of the calculated scattering profile. The resulting models of this process can be seen on fig. 7. If a model overfits the data, we discard it as its complexity may not be physical. We include a zoom of the most dominant magnetic peak to get a better view of the discrepancy between the different fits.

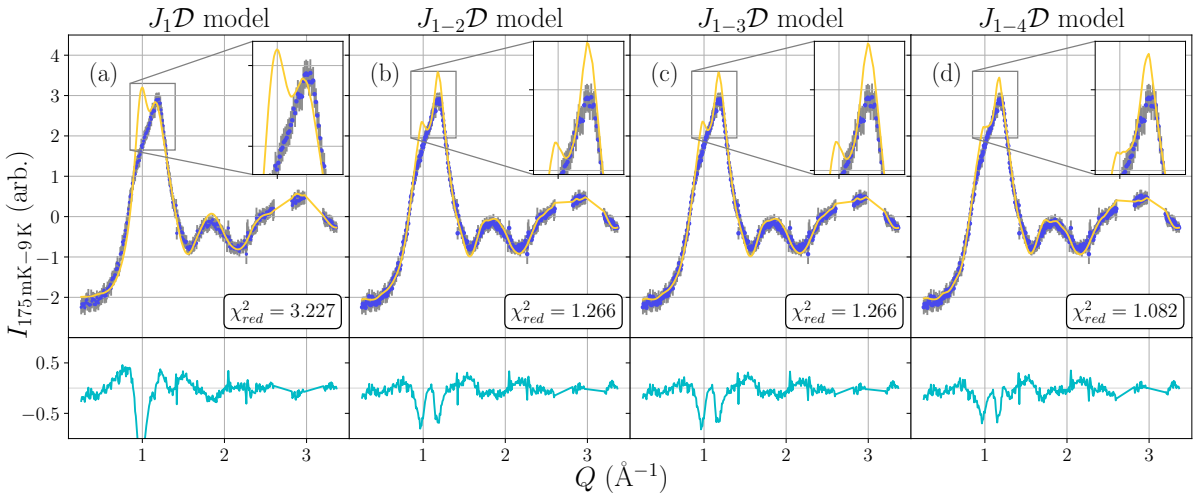

Figure 7: Data and fits of four different models for GGG at $T = 0.175$ K. (a) $J_1\mathcal{D}$ fit, (b) $J_{1-2}\mathcal{D}$ fit, (c) $J_{1-3}\mathcal{D}$ fit, and (d) $J_{1-4}\mathcal{D}$ fit. In the bottom right box is the reduced chi-square value for each fit. Below each graph is a difference curve between fit and data.

This process yielded the $J_{1-4}\mathcal{D}$ model as the best. Having obtained this model, we plot the fits for each temperature used in this refinement along with a difference curve between the fit and data. This is shown in fig. 8.

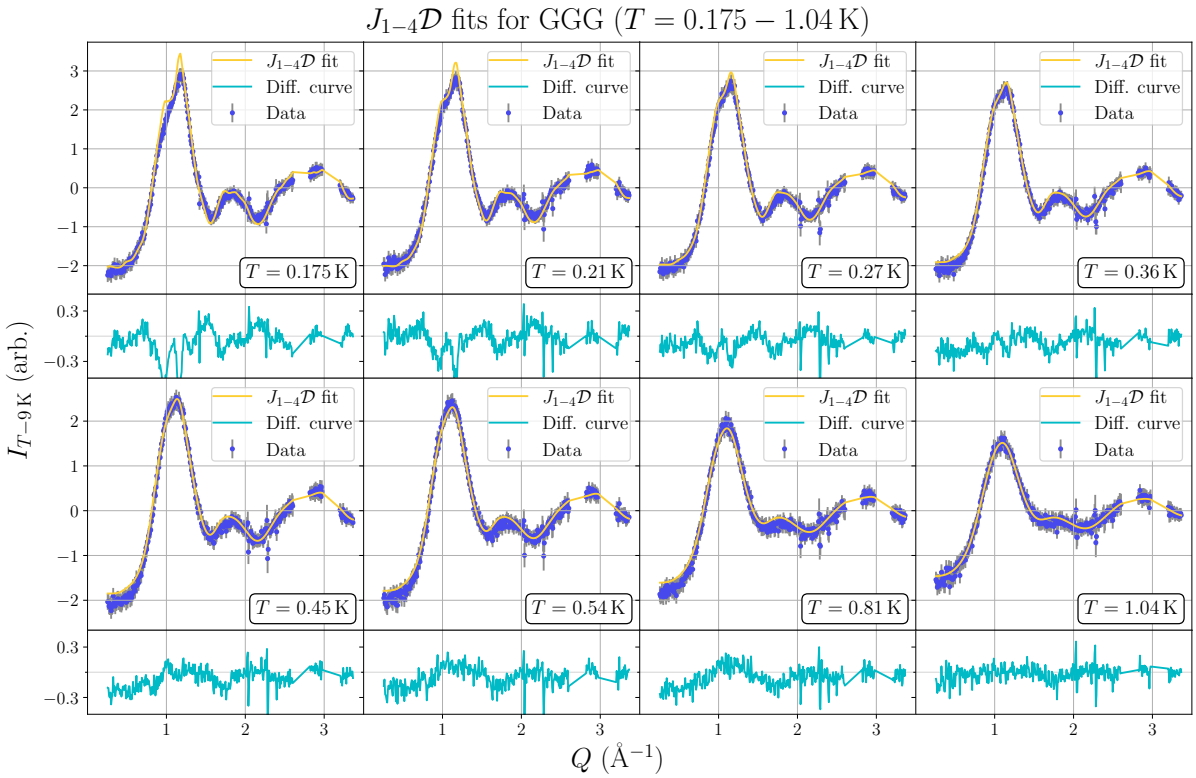

Figure 8: Data and fits for GGG using the $J_{1-4}\mathcal{D}$ model. Eight temperatures between 0.175 and 1.04 K. Below each graph is a difference curve between fit and data.

Finally, the parameter values for each refinement including the insufficient models, the final model, and reference parameter values for comparison are shown in table 3.

$Gd_3Ga_5O_{12}$	J_1(mK)	J_2(mK)	J_3(mK)	J_4(mK)	$\mathcal{D}$ (mK)	χ^2_{red}
Fit $J_1\mathcal{D}$	115 ± 2	0*	0*	0*	45.7*	3.227
Fit $J_{1-2}\mathcal{D}$	117 ± 2	-3.8 ± 0.1	0*	0*	45.7*	1.266
Fit $J_{1-3}\mathcal{D}$	117 ± 2	-3.6 ± 0.2	-1.1 ± 0.7	0*	45.7*	1.266
Fit $J_{1-4}\mathcal{D}$	130 ± 3	-3.9 ± 0.1	4.2 ± 0.7	4.0 ± 0.4	45.7*	1.082
Ref. [9] (2022)	130 ± 2	-3.8 ± 0.1	4.0 ± 0.6	4.0 ± 0.3	45.7*	-
Ref. [15] (2006)	107*	-12:-4	-3:12	0*	45.7*	-

Table 3: Row 1-4: Fitted parameters for GGG with different models. Row 5-6: Parameters from other works. * indicates a fixed parameter. χ^2_{red} is only for $T = 0.175\,\mathrm{K}$.

5.3 Discussion

The fitted parameters for the $J_{1-4}\mathcal{D}$ model in table 3 are almost identical to Paddison's own results from [9]. The small discrepancies are most likely the result of our refinement using a different resolution. Thus, we succeeded in recreating Joe Paddison's results which was one of our goals. This makes sense since we use the same selected data points.

The $J_{1-4}\mathcal{D}$ model is chosen as the model that best describes the data because it shows significant improvement compared to the $J_{1-3}\mathcal{D}$ model. The benefit of considering the extra neighbour is especially apparent at the peak near $Q \approx 1\,\mathrm{Å}^{-1}$ on fig. 7 where the $J_{1-3}\mathcal{D}$ fit lies significantly higher. Furthermore, χ^2_{red} for the $J_{1-4}\mathcal{D}$ model is significantly lower. The $J_{1-5}\mathcal{D}$ model's qualitative improvement in shape and improvement in χ^2_{red} (appendix B) are not significant enough to warrant the extra exchange parameter. All four models in fig. 7 have issues correctly fitting the peak near $Q \approx 1\,\mathrm{Å}^{-1}$ present in the 175 mK data.

Fig. 8 shows the $J_{1-4}\mathcal{D}$-fits for all eight temperatures. The fits nicely cover the data as the distinct magnetic peak to the left and the small magnetic bumps to the right become more pronounced with decreasing temperature. Only the fits for the three lowest temperature data sets have a little bit of trouble covering the left peak as it becomes exceedingly sharp.

Looking to compare our results with other suggested models apart from Paddison's to see how Spinteract holds up to other methods, we look to [15]. They found an optimal model for describing GGG to be a $J_{1-3}\mathcal{D}$-model with parameter values listed in table 3. Comparing their model with our $J_{1-3}\mathcal{D}$, we see that our value for J_1 lies within ten percent of their value for the same parameter. Additionally, our value for J_2 almost lies within the higher part of their estimated interval for J_2 while our J_3 lies within the lower end of their interval for J_3.

We suspect that the reason why the $J_{1-4}\mathcal{D}$ fit does not accurately capture the peak at $Q \approx 1\,\mathrm{Å}^{-1}$ is that the resolution used in Spinteract was too low. A subsequent Spinteract $J_{1-4}\mathcal{D}$ fit was made with 66% more BZ-points (appendix C). However, this yielded almost the exact same interaction parameters and showed no improvement in the shape of the peak. Another explanation is that the spins have entered a state of partial freezing at $T = 0.175\,\mathrm{K}$ and thus are not suitable to be modelled in Spinteract.

6 Ytterbium Gallium Garnet

In this chapter, data analysis and Spinteract refinements of neutron scattering data taken on $Yb_3Ga_5O_{12}$ (YbGG) will be presented and discussed. We use Spinteract to find the optimal

parameters in various Hamiltonians describing the magnetic interactions in YbGG. Additionally, we use Spinteract to recreate other proposed models for YbGG from various literature [8, 11] and compare these with our own results. As mentioned in 2.3.2, the convention used for YbGG will be one where the dipolar interaction parameter is $\mathcal{D} = |J|^2 g_J^2 D_{Dip}$.

6.1 Introduction to YbGG

Cold neutron inelastic scattering spectroscopy was performed in 2017 by Lise Sandberg and Pascale Deen on the CNCS instrument at Oak Ridge National Laboratory in the US on a 1.9 g $Yb_3Ga_5O_{12}$ single-crystal. The experiments were done at sample temperatures of 50 mK and 13 K, with incident energies $E = 1.55$ and 3.32 meV, and energy transfer ranges of $\hbar\omega \in [-0.5 : 1.5]$ meV and $\hbar\omega \in [-1.5 : 3.2]$ meV respectively. The data was first published in [11]. In both experiments, the sample was rotated a total of 180° through the scattering plane comprising (-2H, 2H,0) and (L, L, 2L). These coordinates describe Miller-indices which will be elaborated in the next section.

In YbGG, short range magnetic order appears below 180 mK, and long range magnetic order develops below 54 mK [4]. Even though the authors in [11] hoped to achieve a sample temperature of 50 mK, YbGG is an insulating material and therefore, it is very likely that the sample temperature was higher than that. In the article, they estimate it to be between 100 and 600 mK. This likely puts us above both of the aforementioned ordering temperatures which works out perfectly for this project since Spinteract only handles diffuse scattering data. For the time being, the nominal temperature of the data will still be 50 mK.

The magnetic interactions in YbGG are not as widely studied as those in GGG. In the article by Sandberg et al. [11], they use Monte Carlo simulations based on neutron scattering and magnetic susceptibility measurements to generate two different models, a $J_1\mathcal{D}$ model and a $J_{1-2}\mathcal{D}$ model, which yielded optimal parameter values of $\mathcal{D} = 0.21$ K, $J_1 = 0.6$ K, and $\mathcal{D} = 0.18$ K, $J_1 = 0.72$ K, $J_2 = 0.12$ K respectively. In another study by Lhotel et al. [8], they used a combination of theoretical calculations related to magnetic susceptibility and specific heat measurements and neutron scattering data to conclude that a possible exchange parameter of nearest neighbours does not exceed 5-10% of the dipole parameter, in contrast to the conclusions in [11]. In [4], they find a positive Curie-Weiss temperature which implies ferromagnetic exchange interactions ($J < 0$) in contrast to [11]. Due to the 6-fold symmetry of the Wyckoff group 24c, we expect all scattering due to interactions between Yb^{3+} ions to show the same symmetry. In contrast to GGG, crystal field effects in YbGG motivates varying the dipole exchange parameter rather than keeping it fixed at its theoretical value [11].

6.2 Data preparation

As discussed in section 4, Spinteract requires inelastic data to be energy-integrated for it to be used in the program. Before starting this process, we make cuts of the data at different values of L to determine which energy transfers should be examined. This can be seen in fig. 9. We choose the values of L such that one goes through two Nuclear Bragg peaks and one goes through a high-intensity section of the data.

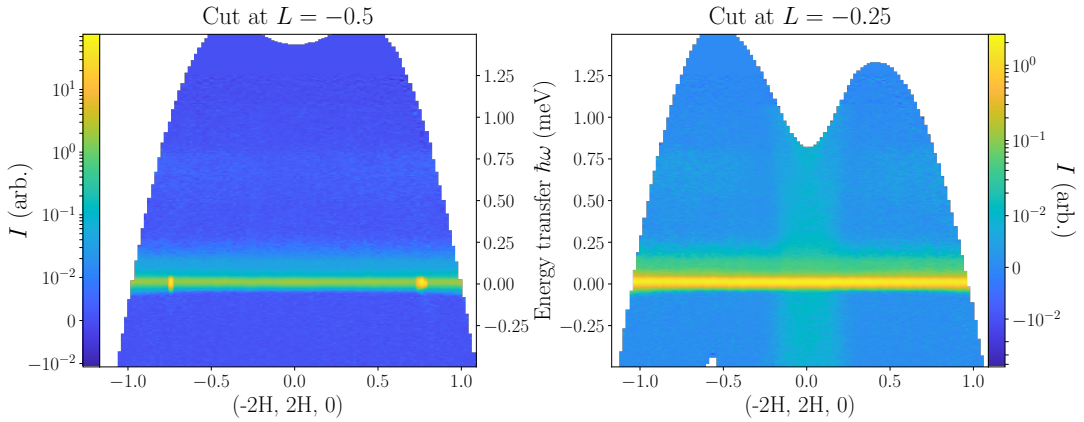

Figure 9: Cuts at different values of L in the data with $E = 1.55\,\text{meV}$. Left: $L = -0.5$. Right: $L = -0.25$. Positive values of $\hbar\omega$ indicate energy transferred to the sample while negative values indicate energy absorbed by the neutron. The $T = 13\,\text{K}$ data has been subtracted. Both graphs have their own logarithmic colormaps.

It is immediately apparent in both cuts on fig. 9 that most scattering occurs around $\hbar\omega \approx 0$. On the left cut with $L = -0.5$, we clearly see the two nuclear Bragg peaks at $H \approx \pm 0.75$. On the right cut with $L = -0.25$, we see a vertical band of intermediate intensity between $H \approx [-0.25 : 0.25]$ across most energy transfers. On both cuts, a low-intensity horizontal band is visible for energy transfers in the range $\hbar\omega \approx [0.5 : 0.75]\,\text{meV}$. The fact that most scattering occurs at $\hbar\omega \approx 0$ motivates not including all energy transfers when energy-integrating. Although, doing this will result in a loss of information present in the horizontal low-intensity band which might show important features. Therefore, we start by calculating the average intensity across all energy transfers. For each scattering vector, we calculate the average intensity

$$I_{total}(\mathbf{Q}) = \frac{1}{N_{\mathbf{Q}}} \sum_i I_i(\mathbf{Q}), \tag{6.1}$$

where $I_i(\mathbf{Q})$ is the intensity measured at the i^{th} energy transfer at scattering vector $\mathbf{Q}$, and $N_{\mathbf{Q}}$ is the number of measurements at that scattering vector. The uncertainty of the total intensity is the individual uncertainties summed in quadrature:

$$\sigma^2_{total}(\mathbf{Q}) = \frac{1}{N_{\mathbf{Q}}} \sum_i \sigma^2_i(\mathbf{Q}), \tag{6.2}$$

where $\sigma_i(\mathbf{Q})$ is the uncertainty of the intensity at scattering vector $\mathbf{Q}$ at the i^{th} energy transfer. This process is carried out for all scattering vectors, $\mathbf{Q}$, both at 50 mK and 13 K for each incident energies and will be labelled as $I_{50\,\text{mK}}(\mathbf{Q})$ with $\sigma_{50\,\text{mK}}(\mathbf{Q})$ and $I_{13\,\text{K}}(\mathbf{Q})$ with $\sigma_{13\,\text{K}}(\mathbf{Q})$ respectively. This can be seen for the 50 mK data with incident energy $E = 1.55\,\text{meV}$ in fig. 10.

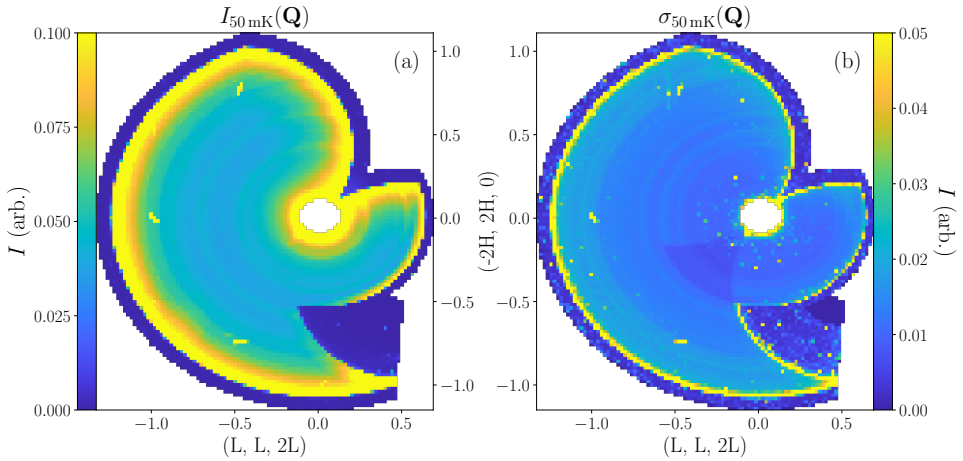

Figure 10: (a) $I_{50\ \mathrm{mK}}(\mathbf{Q})$ using eq. (6.1). (b) $\sigma_{50\ \mathrm{mK}}(\mathbf{Q})$ using eq. (6.2). Incident energy of $E = 1.55\,\mathrm{meV}$. All 400 energy transfers used. Notice how the intensity scales are different for the two graphs, and how they share the vertical axis.

The axes on fig. 10 denote Miller-indices. For example, the point $(L,\, H) = (-1.0,\, 0.5)$ is converted to a Miller-index by inserting -1 for L and 0.5 for H. This results in $(h,\, k,\, l) = (-1,\, -1,\, -2) + (-1,\, 1, 0) = (-2,\, 0, -2)$, so $(hkl) = (\bar{2}0\bar{2})$.

During a neutron scattering experiment, a variety of scattering occurs; not only magnetic. For this reason, a high temperature measurement, in this case 13 K, is subtracted from the 50 mK data. It can be safely assumed that at 13 K, YbGG is well into its paramagnetic regime because 13 K is far above YbGG's magnetic ordering temperature as discussed in section 2.3.1. The idea is that the difference between the two data sets only shows the magnetic features produced from the geometric frustration. The intensity can now be calculated as follows:

$$I_{50\,\mathrm{mK}-13\,\mathrm{K}}(\mathbf{Q}) = I_{50\,\mathrm{mK}}(\mathbf{Q}) - I_{13\,\mathrm{K}}(\mathbf{Q}) \tag{6.3}$$

with uncertainties:

$$\sigma_{50\,\mathrm{mK}-13\,\mathrm{K}}(\mathbf{Q}) = \sqrt{\sigma_{50\,\mathrm{mK}}(\mathbf{Q})^2 + \sigma_{13\,\mathrm{K}}(\mathbf{Q})^2}. \tag{6.4}$$

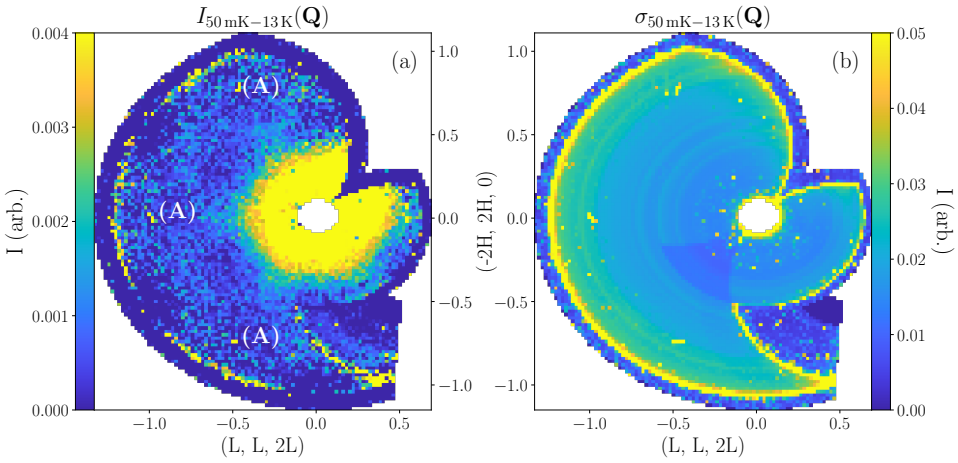

Figure 11: (a) $I_{50\,\mathrm{mK}-13\,\mathrm{mK}}(\mathbf{Q})$ using eq. (6.3). (b) $\sigma_{50\,\mathrm{mK}-13\,\mathrm{K}}(\mathbf{Q})$ using eq. (6.4). (A) Nuclear Bragg peaks to be removed. Incident energy of $E = 1.55\,\mathrm{meV}$. All 400 energy transfers used.

After subtracting the 13 K measurement, not all data is useful. In fig. 11 (a), we see three obvious nuclear Bragg peaks, each marked with an (A). Additionally at the edge, we see an oval shape of high intensity followed by almost no intensity extending further out. This is clearly not physical and is likely the result something weird happening at the edge of the detector. Finally, a few data points of low intensity close to the center are clearly the result of erroneous measurements. For these reasons, we remove all data points which are likely not caused by magnetic scattering. We deem it more harmful to leave in erroneous data than to delete minimal suitable data. We call this data $S_{mag}(\mathbf{Q})$ as all the intensity should stem from magnetic interactions.

Looking at $S_{mag}(\mathbf{Q})$ in fig. 12 (a), it is hard to see any structure outside of the high-intensity center. For this reason, an (almost) elastic data set, $S_{elas}(\mathbf{Q})$, is created only using data from the eight lowest values of $|\hbar\omega|$. This range was chosen by examining fig. 9 as well as looking at cuts for different values of $\hbar\omega$. These eight lowest values lie in the range $-0.0175\,\mathrm{meV} \leq \hbar\omega \leq 0.0175\,\mathrm{meV}$. This can be seen on fig. 12 (b).

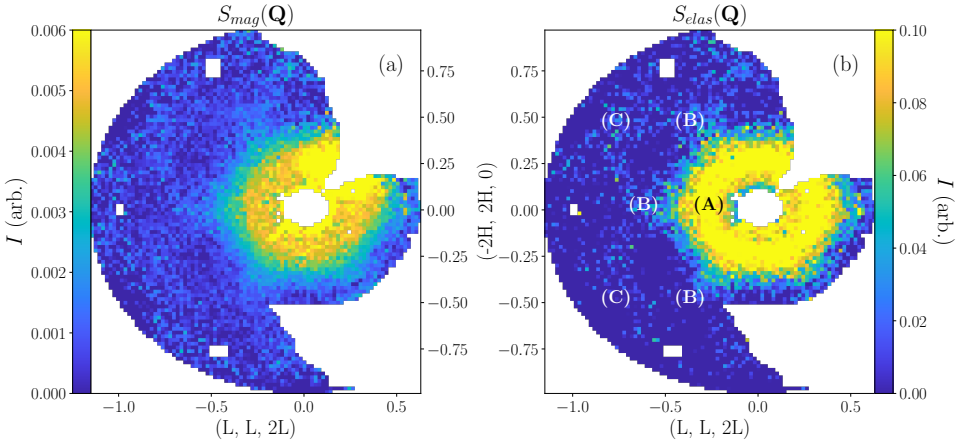

Figure 12: (a) $S_{mag}(\mathbf{Q})$. Nuclear Bragg peaks and non-magnetic data removed. All 400 energy transfers used. (b) $S_{elas}(\mathbf{Q})$. Same points removed as in (a), data for $|\hbar\omega|$ in range $-0.0175\,\mathrm{meV} \leq \hbar\omega \leq 0.0175\,\mathrm{meV}$. (A) High-intensity hexagonal center. (B) Sections connecting the high-intensity center to higher Q features. (C) Low-intensity band at higher Q. Incident energy of $E = 1.55\,\mathrm{meV}$.

In $S_{elas}(\mathbf{Q})$, we see features outside the center which appear to show the expected 6-fold symmetry. Furthermore, the center is more well-defined and clearly shows the 6-fold symmetry as opposed to $S_{mag}(\mathbf{Q})$, where the structure is almost circular with a deformity in the top right. For both $S_{mag}(\mathbf{Q})$ and $S_{elas}(\mathbf{Q})$, the uncertainties are roughly an order of magnitude larger than the intensities which is concerning. This is due to the fact that the differences between the 50 mK intensities and the 13 K intensities are, in general, smaller than the respective uncertainties. This will be elaborated in section 6.4. We notice three important features in $S_{elas}(\mathbf{Q})$: (A) The high-intensity hexagonal center, (B) intermediate-intensity sections at the corners of the hexagon, connecting it to the low-intensity features at higher Q, and (C) a low-intensity band at higher Q that runs around the entire center. When comparing the data to various models in the upcoming sections, these features are especially important.

We use the exact same procedure for the data with incident energy $E = 3.32\,\text{meV}$ which we will always denote as $E = 3.32\,\text{meV}$. This is shown in fig. 13. These data were only recorded in 100 discrete energy transfers (as opposed to 400), and we select $S_{elas}(\mathbf{Q})$ ($E = 3.32\,\text{meV}$) such that $\hbar\omega$ has a range of $-0.184\,\text{meV} \leq \hbar\omega \leq 0.145\,\text{meV}$. The advantage of only using the elastic data is not as obvious here as for $E = 1.55\,\text{meV}$. Furthermore, the structure seen in fig. 12 (b) cannot be noticeably recognized in fig. 13 (b). All in all, the $E = 3.32\,\text{meV}$ data seems to be far more noisy than the $E = 1.55\,\text{meV}$ data. For these reasons, we will be modelling the two data sets separately.

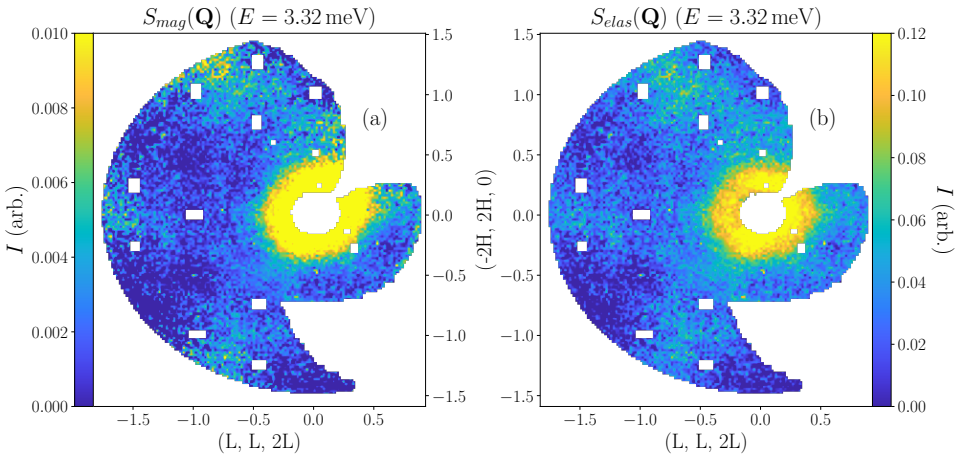

Figure 13: (a) $S_{mag}(\mathbf{Q})$ ($E = 3.32\,\text{meV}$). Nuclear Bragg peaks and non-magnetic data removed. All 100 energy transfers used. (b) $S_{elas}(\mathbf{Q})$ ($E = 3.32\,\text{meV}$). Same points removed as in (a), only data for eight lowest values of $|\hbar\omega|$ used with $-0.184\,\text{meV} \leq \hbar\omega \leq 0.145\,\text{meV}$.

6.3 Modelling in Spinteract

In Spinteract, the user supplies the sample temperature at which the data was recorded. This raises an issue as the exact sample temperature of our YbGG data is unknown. Varying the temperature in Spinteract using an upper and lower bound of 0.1 K and 0.6 K produces widely different results. The aim of refining precise interaction parameters can thus no longer be achieved. However, we still hope to compare the qualitative effects of including exchange parameters in the model as discussed in section 6.1. Determining whether a model including only the dipole interaction is sufficient to describe the data is especially of interest.

6.3.1 $E = 1.55\,\mathbf{meV}$ data

For all models fitted or calculated, we will compare with the data in the top half of the figure. Due to the large uncertainties (see fig. 11 (b)), the values of χ^2_{red} are very small, ~ 0.05, and do not seem to reflect the overall quality of the fits. For this reason, we have not included them. Initially, we produce 3 fits with $\mathcal{D}$, $J_1\mathcal{D}$ and $J_{1-2}\mathcal{D}$ models in Spinteract. These are shown in fig. 14 and fig. 15 with $T = 250\,\text{mK}$ and 450 mK respectively. The default sample temperature is $T = 250\,\text{mK}$, and the sample temperature will only be mentioned explicitly if it is not $T = 250\,\text{mK}$.

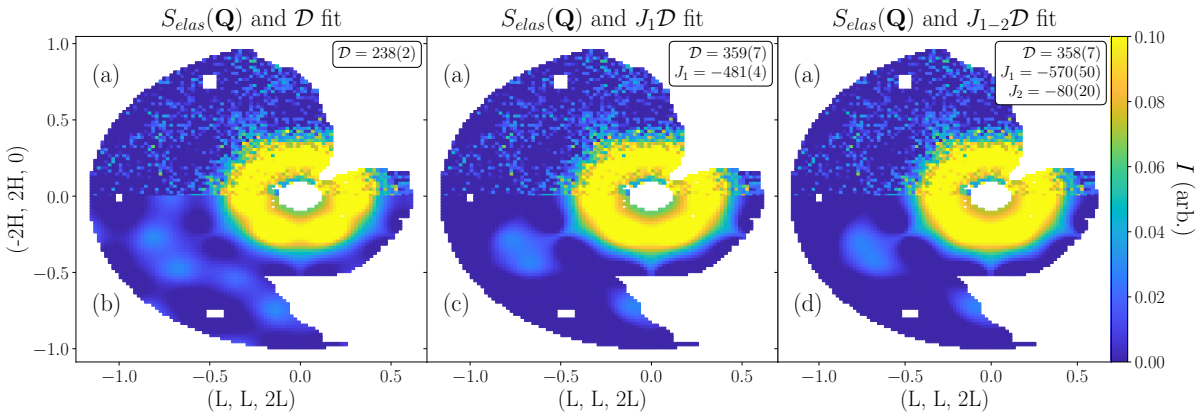

Figure 14: (a) $S_{elas}(\mathbf{Q})$. Spinteract fits with (b) $\mathcal{D}$ fit, (c) $J_1\mathcal{D}$ fit, and (d) $J_{1-2}\mathcal{D}$ fit. Incident energy of $E = 1.55\,\text{meV}$. Numbers in top right boxes show fitted interaction parameters and have units of mK. Number in parentheses indicate $\pm$ uncertainty.

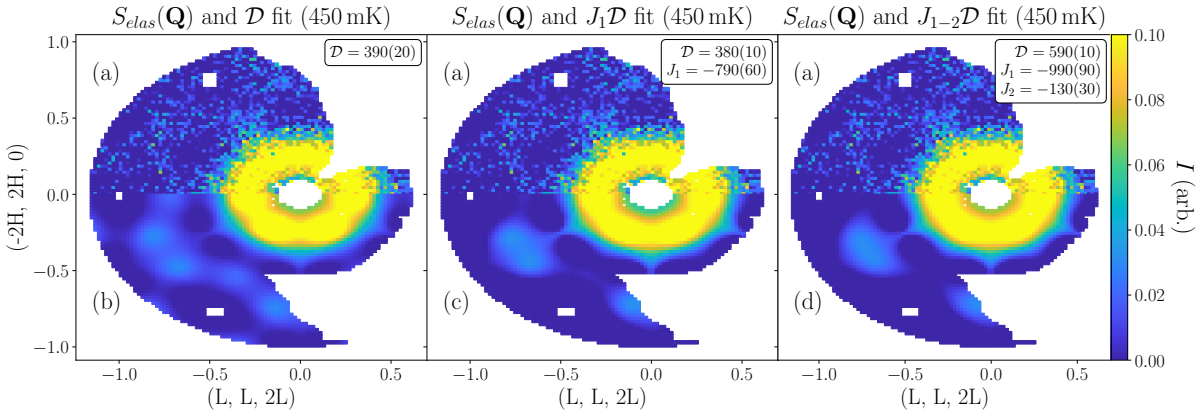

Figure 15: (a) $S_{elas}(\mathbf{Q})$. Spinteract fits with (b) $\mathcal{D}$ fit, (c) $J_1\mathcal{D}$ fit, and (d) $J_{1-2}\mathcal{D}$ fit. Incident energy of $E = 1.55\,\text{meV}$. Numbers in top right boxes show fitted interaction parameters and have units of mK. Number in parentheses indicate $\pm$ uncertainty. $T = 450\,\text{mK}$

Comparing the three fits with $T = 250\,\text{mK}$ in fig. 14 with the data, all three fits reproduce the hexagonal center, though models containing exchange interaction parameters J_1 or J_{1-2} fail to capture additional details in the high Q sections of the data. Instead, the fit containing only the dipolar interaction more accurately captures the lower intensity features around the high-intensity center. Furthermore, the value for $\mathcal{D}$ in this fit is much closer to the theoretical value calculated in table 2 ($\mathcal{D} = 245.6\,\text{mK}$) than the value found in the other two fits.

The same qualitative differences between fits and data can be seen for the results with the sample temperature set at $T = 450\,\text{mK}$ in fig. 15, though the parameter value for $\mathcal{D}$ in each fit is far too high compared to the expected theoretical value. This results in further confidence that the actual sample temperature was closer to 250 mK than 450 mK. For this reason, the sample temperature will be fixed at 250 mK in the remaining fits and models we present in this chapter.

Next, we examine the models proposed in [11] and described in section 6.1, which we will denote (Sandberg). The models are calculated with Spinteract and can be seen in fig. 16.

To investigate whether the anisotropic g-factor, as introduced in eq. (2.1), is required to describe the neutron scattering data, we also create a model using the angular averaged $g \approx 3.42$ in a $\mathcal{D}$ model, where we fix $\mathcal{D} = 238\,\text{mK}$. This can be seen in fig. 16.

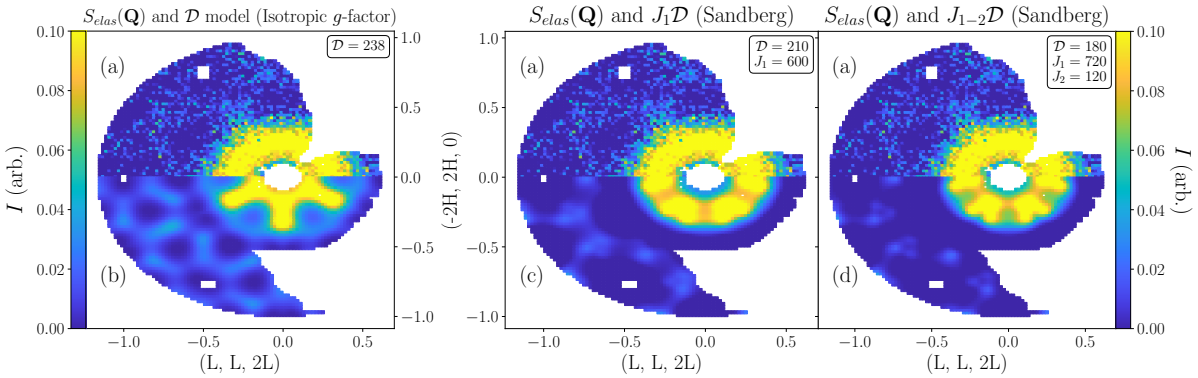

Figure 16: (a) $S_{elas}(\mathbf{Q})$. (b) Calculated $\mathcal{D}$ model with an isotropic g-factor. (c-d) Models from [11] calculated, not fitted, with Spinteract (c) $J_1\mathcal{D}$ model, (d) $J_{1-2}\mathcal{D}$ model. Incident energy of $E = 1.55\,\text{meV}$.

The model including an isotropic g-factor in fig. 16 (b) does not reproduce the data very well. The center is no longer hexagonal, and the higher Q features look nothing like those in the data. Looking at fig. 16 (c-d), both models from [11] somewhat reproduce the shape of the original data though they both fail at replicating the short low-intensity segments connecting the hexagonal center to the higher Q features further out. The $J_1\mathcal{D}$ model captures the hexagon and higher Q features slightly better than the one including an additional exchange constant J_2. Furthermore, the value of $\mathcal{D}$ is closer to the theoretical value in the $J_1\mathcal{D}$ model than in the $J_{1-2}\mathcal{D}$ model.

To investigate the claim that J_1 lies within $5-10\%$ of $\mathcal{D}$ from [8], we calculate models with varying values of J_1. We use the value of $\mathcal{D} = 238\,\text{mK}$ found in fig. 14 (b). Both positive and negative values of J_1 are considered in fig. 17 and fig. 18 respectively. Models where $J_1 = \pm 2\mathcal{D}/g_J^2$ are considered in appendix E.

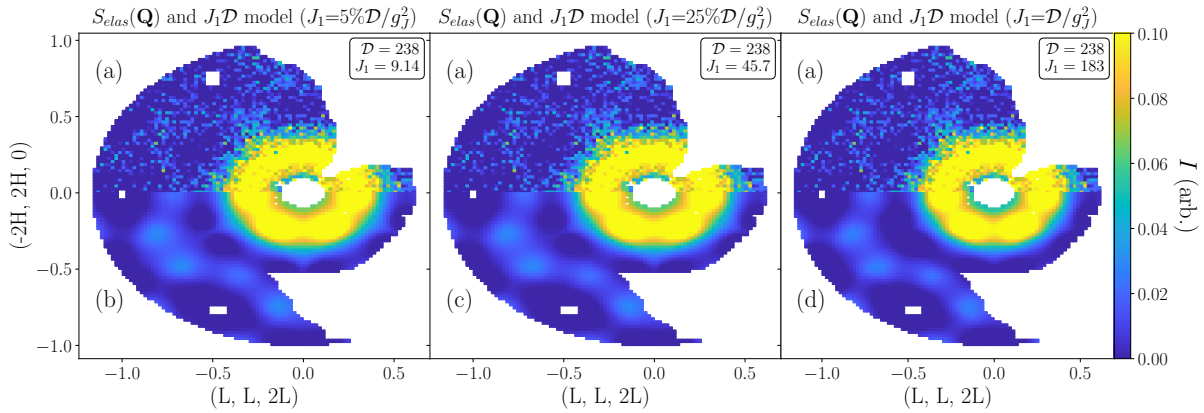

Figure 17: (a) $S_{elas}(\mathbf{Q})$. $J_1\mathcal{D}$ models calculated, not fitted, with Spinteract for varying J_1 with (b) $J_1 = 5\%\mathcal{D}/g_J^2$, (c) $J_1 = 25\%\mathcal{D}/g_J^2$, and (d) $J_1 = \mathcal{D}/g_J^2$. Incident energy of $E = 1.55\,\text{meV}$.

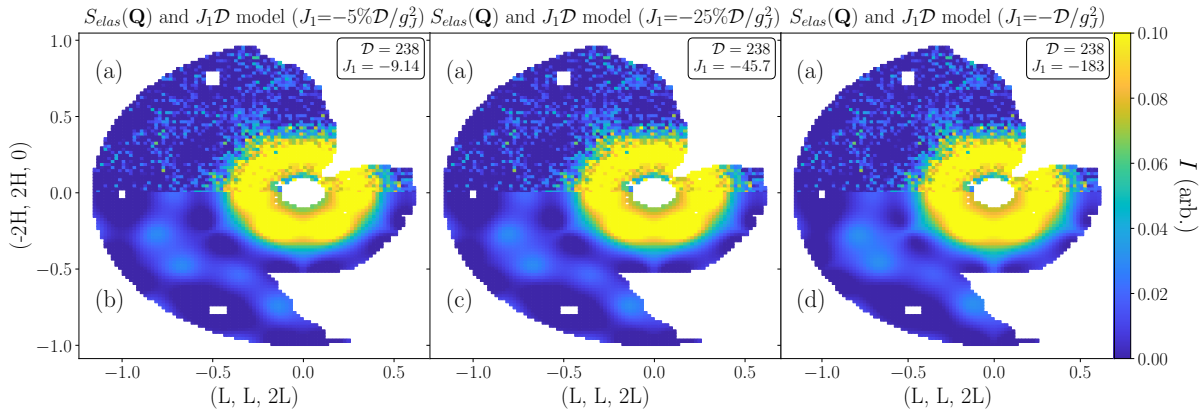

Figure 18: (a) $S_{elas}(\mathbf{Q})$. $J_1\mathcal{D}$ models calculated, not fitted, with Spinteract for varying J_1 with (b) $J_1 = -5\%\mathcal{D}/g_J^2$, (c) $J_1 = -25\%\mathcal{D}/g_J^2$, and (d) $J_1 = -\mathcal{D}/g_J^2$. Incident energy of $E = 1.55\,\text{meV}$.

Looking at fig. 17 and fig. 18, it is not immediately apparent which model best describes the data as different models capture distinct features of data better or worse than the rest. Comparing the models for $J_1 = \pm\mathcal{D}/g_J^2$ in fig. 17 (d) and fig. 18 (d), the latter has a more pronounced high-intensity hexagonal center, and does a better job at replicating the more diffuse low-intensity features of the data. Additionally, it captures the connecting segments between the inner high-intensity features and the surrounding low-intensity features. However in both cases, the model with lower $|J_1|$ seems do a better job in all of these aspects.

The models where $J_1 = \pm 25\%\mathcal{D}/g_J^2$ in fig. 17 (c) and fig. 18 (c) only have subtle though important differences. They both accurately capture the high-intensity center. However, the one with negative J_1 more accurately depicts the sections connecting the center to the higher Q features.

The models where $J_1 = \pm 5\%\mathcal{D}/g_J^2$ in fig. 17 (b) and fig. 18 (b) are essentially identical. Furthermore, they look very similar to the models where $J_1 = \pm 25\%\mathcal{D}/g_J^2$.

To better compare the different models, we make vertical one-dimensional (1D) cuts through the data and selected models. For the latter, we choose three good candidates: The $\mathcal{D}$ fit from fig. 14 (b), the $J_1\mathcal{D}$ model ($J_1 = -25\%\mathcal{D}/g_J^2$) from fig. 18 (c), and the $J_1\mathcal{D}$ model (Sandberg) [11]

from fig. 16 (c). We decide to make the cut at $L = -0.31$ as this should cover all the important features of the data: The center hexagon, higher Q features, and the sections connecting them (as explained on fig. 12 (b)). These cuts can be seen on fig. 19. Uncertainties are not included as these are orders of magnitude larger than the intensities.

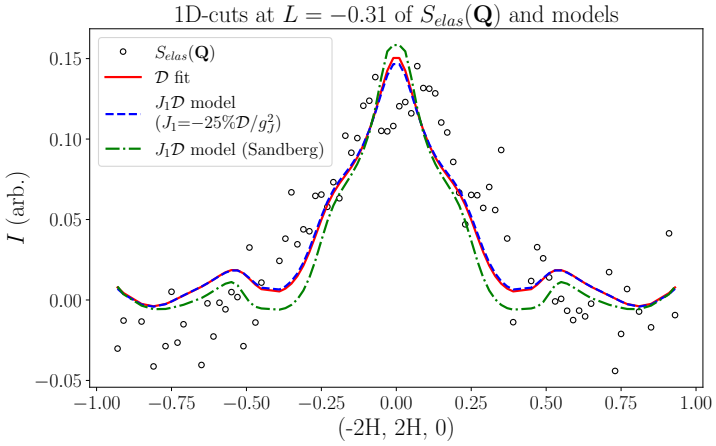

Figure 19: 1D-cuts through $L = -0.31$ of $S_{elas}(\mathbf{Q})$ (black circles), $\mathcal{D}$ fit from fig. 14 (b) (in red), $J_1\mathcal{D}$ model ($J_1 = -25\%\mathcal{D}/g_J^2$) from fig. 18 (c) (in blue), and the $J_1\mathcal{D}$ model (Sandberg) [11] from fig. 16 (c) (in green).

It is immediately apparent that including the small exchange interaction makes almost no difference to the calculated intensities. Only at $H = 0$ does the model with $J_1 = -25\%\mathcal{D}/g_J^2$ produce slightly higher intensities. The $J_1\mathcal{D}$ model (Sandberg) produces a noticeably higher peak at low Q and significantly lower valleys in the ranges $H \approx [-0.5; -0.3]$ and $[0.3; 0.5]$.

6.3.2 $E = 3.32$ meV data

In this section, we model $S_{mag}(\mathbf{Q})$ ($E = 3.32$ meV) and $S_{elas}(\mathbf{Q})$ ($E = 3.32$ meV). We produce 3 fits with $\mathcal{D}$, $J_1\mathcal{D}$, and $J_{1-2}\mathcal{D}$ models for each data set. Results for $S_{mag}(\mathbf{Q})$ ($E = 3.32$ meV) are included in fig. 20 below whereas results for the elastic set are put in appendix F.

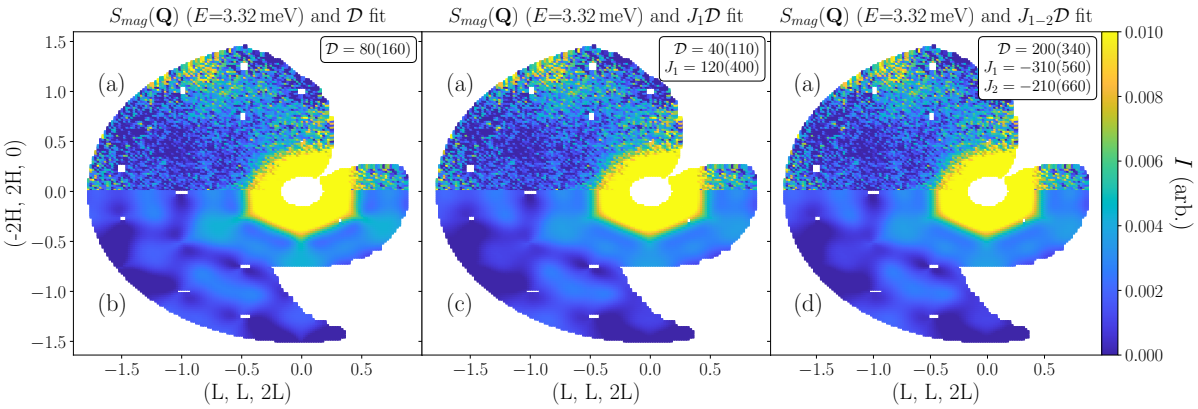

Figure 20: (a) $S_{mag}(\mathbf{Q})$ ($E = 3.32$ meV). Spinteract fits with (b) $\mathcal{D}$ fit, (c) $J_1\mathcal{D}$ fit, and (d) $J_{1-2}\mathcal{D}$ fit. Numbers in top right boxes show fitted interaction parameters and have units of mK. Number in parentheses indicate ± uncertainty.

The parameters found in fig. 20 all have very high uncertainties, which essentially makes them useless. Additionally, they do not seem to agree very well with the ones found for $S_{elas}(\mathbf{Q})$ in fig. 14. All three models rotate the hexagon in the center by 30° compared to fig. 14. The higher Q sections of the fits all seem to depict the data adequately although as discussed in section 6.1, the lack of detailed resolution in the data makes it difficult to say anything meaningful about the qualitative resemblance between the data and the different fits. The models deemed the best candidates for describing the $E = 1.55\,\text{meV}$ data were the $\mathcal{D}$ fit from fig. 14 (b) and the model where $J_1 = -25\%\mathcal{D}/g_J^2$ from fig. 18 (c). These models are calculated for $S_{elas}(\mathbf{Q})$ ($E = 3.32\,\text{meV}$) and can be seen in fig. 21.

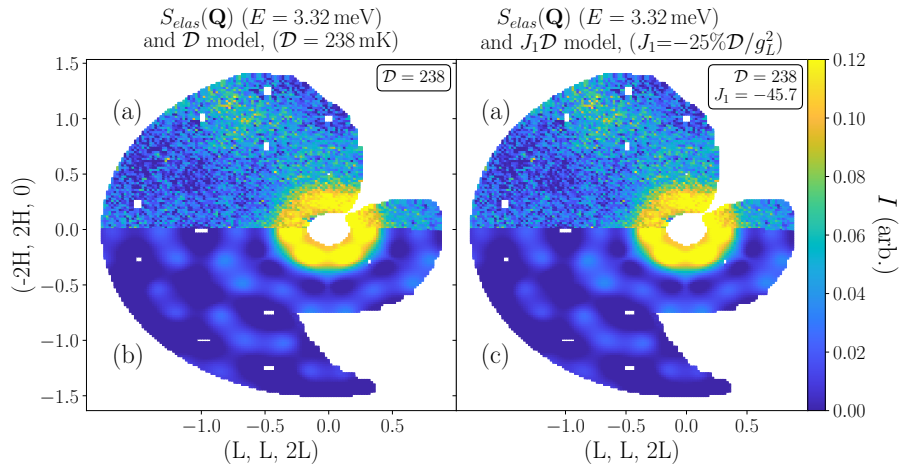

Figure 21: (a) $S_{elas}(\mathbf{Q})$ ($E = 3.32\,\text{meV}$). Spinteract fit/model with (b) $\mathcal{D}$ fit from fig. 14 (b), and (c) $J_1\mathcal{D}$ model from fig. 18 (c). Numbers in top right boxes show fitted interaction parameters and have units of mK.

At these high Q values, including an exchange parameter J_1 in fig. 21 becomes less noticeable. The noisy data makes it difficult to conclude anything about the quality of the models.

6.4 Discussion

We have used Spinteract to fit and calculate various models to neutron scattering data for YbGG with an estimated sample temperature of 0.250 and 0.450 K. For the data with $E = 1.55\,\text{meV}$, we produced fits for three different magnetic Hamiltonians including 1) a dipolar term, $\mathcal{D}$, 2) a $\mathcal{D}$-term and a nearest neighbour exchange term, J_1, and finally 3) a $\mathcal{D}$-term and exchange terms between nearest and next nearest neighbours, J_1 and J_2. In the case where the sample temperature was set to 0.250 K, the fit only including the dipolar term was found to be the optimal one capturing both the qualitative features of the data while also providing an estimate of $\mathcal{D}$ close to the expected theoretical value. In the case where the temperature was set to 0.450 K, roughly the same qualitative features were seen, but the parameters were higher than expected. This motivated only estimating the sample temperature to be 0.250 K moving forward.

Next, we recreated the $J_1\mathcal{D}$ and $J_{1-2}\mathcal{D}$ models found in [11]. The models adequately capture the low- and high-Q regime though both have room for improvement in the sections connecting the center to the higher Q parts of the data.

Then, we made models with varying J_1 and found that including $J_1 = \pm 5\%\mathcal{D}/g_J^2$ essentially makes no difference to the shape of the model compared to one only including $\mathcal{D}$. Differences

begin to be noticeable when increasing the nearest neighbour exchange parameter to $J_1 = \pm 25\%\mathcal{D}/g_J^2$. The models with $J_1 = \pm\mathcal{D}/g_J^2$ are found to be qualitatively worse than the ones with $J_1 = \pm 25\%\mathcal{D}/g_J^2$. In general, the negative sign on J_1 seems to make the features more diffuse, while the positive sign "streamlines" the higher Q parts. All in all in a $J_1\mathcal{D}$ model with $\mathcal{D} \approx 240\,\text{mK}$, we estimate that the value for J_1 which best recreates the data is in the range $-\mathcal{D}/g_J^2 < J_1 < -25\%\mathcal{D}/g_J^2$, indicative of ferromagnetic interactions. The low-magnitude J_1 and negative sign is in stark contrast to the $J_1\mathcal{D}$ and $J_{1-2}\mathcal{D}$ models from [11]. However, our results agree with those reported in [4, 8] that found a positive Curie-Weiss temperature indicative of ferromagnetic interactions. Additionally, our relatively low estimate of the magnitude of J_1 does not stray too far from the claim that J_1 does not exceed 5-10% of $\mathcal{D}$ from [8], although the effects of including such a small J_1 are negligible.

The quality of the data, both with $E = 1.55$ and especially with $E = 3.32\,\text{meV}$, makes direct fitting of exchange interaction parameters unfeasible. This is likely because too much emphasis is put on the low-Q center where intensities are much greater than in the high-Q regions. The features present at higher Q suffer from a lot of noise, making it difficult to distinguish significant qualitative details from insignificant ones. As such, we cannot exclude the possibility that a more complex magnetic Hamiltonian is needed to describe YbGG.

In order to use Spinteract to model YbGG, we have made the assumption that a semiclassical method is sufficient to describe the magnetic interactions in this system. This was a potential pitfall due to YbGG being a correlated quantum system with effective spin-$\frac{1}{2}$. However, our models containing only the dipolar interaction or this plus a low-magnitude nearest neighbour exchange interaction adequately reproduce the qualitative features of the data and concur with our theoretical estimate of the value for $\mathcal{D}$. These results build confidence that a semiclassical assumption can be justified. Implementating an anisotropic g-factor was found to be crucial for reproducing the scattering intensities.

7 Conclusion and outlook

We have analysed magnetic diffuse scattering data from two different neutron scattering experiments taken on the highly frustrated rare earth garnets GGG and YbGG, and modelled the magnetic interactions in these compounds using the newly-developed program Spinteract. After reproducing results created in this program for the well-studied magnetic interactions in GGG, we succesfully used Spinteract to investigate various magnetic Hamiltonians for YbGG.

Comparing our own original fits and several proposed models calculated in Spinteract, we conclude that a Hamiltonian containing only a dipolar interaction of magnitude $\mathcal{D} = 238\,\text{mK}$ or potentially also including a nearest neighbour exchange term with a strength in the range $[-\mathcal{D}/g_J^2, -25\%\mathcal{D}/g_J^2]$ is able to give a qualified description of the magnetic interactions in YbGG.

To gain further insight into the magnetic interactions of the highly frustrated YbGG, we would like to analyse more neutron scattering data taken on this material. We only had access to two of the three Q-dimensions, although a third dimension of data from this exact experiment does exist, and it would be interesting to extent our analysis to include this as well. Furthermore, we have observed how Spinteract is highly temperature-dependent. Performing a new neutron scattering experiment on a YbGG powder sample rather than on a single crystal would achieve a more reliable sample temperature and thus, more confident results could be generated using Spinteract.

References

[1] S. Blundell, *Magnetism in Condensed Matter*, Oxford University Press, 1st edition, 2001, ISBN: 978 0 19 850592 1

[2] A. T. Boothroyd, *Principles of Neutron Scattering from Condensed Matter*, Oxford University Press, 1st edition, 2020, ISBN: 978 0 19 886231 4

[3] P. P. Deen, An overview of the director state in gadolinium gallate garnet, *Front. Phys.* **10**, 2022

[4] J. Filippi, J. C. Lasjaunias, B. Hebral, J. Rossat-Mignod, and F. Tcheou, Magnetic properties of ytterbium gallium garnet between 44 mK and 4K, *J. Phys. C: Solid State Phys.* **13**, 1277, 1980

[5] D. J. Griffiths, and D. F. Schroeter, *Introduction to Quantum Mechanics*, Cambridge University Press, 3rd edition, 2018, ISBN: 978 1 107 18963 8

[6] H. Jacobsen, O. Florea, E. Lhotel, K. Lefmann, O. A. Petrenko, C. S. Knee, T. Seydel, P. F. Henry, R. Bewley, D. Voneshen, A. Wildes, G. Nilsen, and P. P. Deen, Spin dynamics of the director state in frustrated hyperkagome systems, *Phys. Rev. B* **104**, 054440, 2021

[7] K. Lefmann, *Neutron Scattering: Theory, Instrumentation, and Simulation*, University of Copenhagen (Version from. 6. march 2023)

[8] E. Lhotel, L. Mangin-Thro, E. Ressouche, P. Steffens, E. Bichaud, G. Knebel, J.-P. Brison, C. Marin, S. Raymond, and M. E. Zhitomirsky, Spin dynamics of the quantum dipolar magnet $Yb_3Ga_5O_{12}$ in an external field, *Phys. Rev. B* **104**, 024427, 2021

[9] J. A. M. Paddison, Spinteract: A Program to Refine Magnetic Interactions to Diffuse Scattering Data, arXiv: `arXiv:2210.09016`, 2022

[10] O. A. Petrenko, C. Ritter, M. Yethiraj, and D. McK Paul, Investigation of the Low-Temperature Spin-Liquid Behavior of the Frustrated Magnet Gadolinium Gallium Garnet, *Phys. Rev. Lett.* **80**, 4570, 1998

[11] L. Ø. Sandberg, R. Edberg, I. B. Bakke, K. S. Pedersen, M. C. Hatnean, G. Balakrishnan, L. Mangin-Thro, A. Wildes, B. Fåk, G. Ehlers, G. Sala, P. Henelius, K. Lefmann, and P. P. Deen, Emergent magnetic behaviour in the frustrated $Yb_3Ga_5O_{12}$, *Phys. Rev. B* **104**, 064425, 2021

[12] L. Ø. Sandberg, *Magnetic Frustration under Pressure*, Niels Bohr Institute, University of Copenhagen, 2022

[13] P. Schiffer, A. P. Ramirez, D. A. Huse, P. L. Gammel, U. Yaron, D. J. Bishop, and A. J. Valentino, Frustration Induced Spin Freezing in a Site-Ordered Magnet: Gadolinium Gallium Garnet, *Phys. Rev. Lett.* **74**, 2379, 1995

[14] Steven H. Simon, *The Oxford Solid State Basics*, Oxford University Press, 1st edition, 2019, ISBN: 978 0 19 968076 4

[15] T. Yavors'kii, M. Enjalran, and M. J. P. Gingras, Spin Hamiltonian, Competing Small Energy Scales, and Incommensurate Long-Range Order in the Highly Frustrated $Gd_3Ga_5O_{12}$ Garnet Antiferromagnet, *Phys. Rev. Lett.* **97**, 267203, 2006

Appendix A Full derivation of dispersion relation

The following is a more thorough derivation of the dispersion relation found in section 2.4 for spin waves in a simple 1D ferromagnet. The derivation is based on the ones found in [1, 14]. We assume a Heisenberg Hamiltonian only with nearest neighbour interactions,

$$\hat{\mathcal{H}} = -2J \sum_{\langle i,j \rangle} \hat{\mathbf{S}}_i \cdot \hat{\mathbf{S}}_j. \tag{A.1}$$

Next, we can use the Heisenberg equations of motion for any operator $\hat{Q}$ [5] from quantum, mechanics

$$i\hbar \frac{d\hat{Q}}{dt} = [\hat{Q}, \hat{\mathcal{H}}], \tag{A.2}$$

to calculate the motion of a spin, $\hat{\mathbf{S}}_p = (S_p^x, S_p^y, S_p^z)$, in such a system. The index p is used as to not confuse it with the imaginary unit. If we only consider spin p, the sum over p disappears from the Hamiltonian, and we only need to consider $j = p-1$ and $p+1$. Furthermore, we use the relation:

$$[S^x, S^y] = i\hbar \varepsilon_{xyz} S^z, \tag{A.3}$$

where ε_{xyz} is the Levi-Civita epsilon. We start by computing the equation of motion for S_p^x:

$$\begin{aligned}
i\hbar \frac{dS_p^x}{dt} &= [S_p^x, \hat{\mathcal{H}}] && \text{(A.4)}\\
&= [S_p^x, -2J \sum_{\langle j \rangle} \hat{\mathbf{S}}_p \cdot \hat{\mathbf{S}}_j] && \text{(A.5)}\\
&= [S_p^x, -2J \sum_{\langle j \rangle} S_p^x S_j^x + S_p^y S_j^y + S_p^z S_j^z] && \text{(A.6)}\\
&= -i2J \sum_{\langle j \rangle} (S_p^z S_j^y - S_p^y S_j^z), && \text{(A.7)}
\end{aligned}$$

where eq. (A.3) was used in the last step. By doing the same for S_p^y and S_p^z, it should become apparent that:

$$\hbar \frac{d\hat{\mathbf{S}}_p}{dt} = 2J \hat{\mathbf{S}}_p \times (\hat{\mathbf{S}}_{p-1} + \hat{\mathbf{S}}_{p+1}). \tag{A.8}$$

Now, if we assume that all spins are aligned along the z-direction in the ground state, we can model small excitations as perturbations. For simplicity's sake, we consider a small excitaion such that $S_p^z = S$, and $S_p^x = \delta S_p^x, S_p^y = \delta S_p^y$, where $|\delta S_p^x|, |\delta S_p^y| \ll |S|$ (likewise for the other sites). If we only keep terms that are linear in δS_p^x and δS_p^y, we obtain:

$$\begin{aligned}
\frac{d\delta S_p^x}{dt} &= \frac{2JS}{\hbar}(2\delta S_p^y - \delta S_{p-1}^y - \delta S_{p+1}^y), && \text{(A.9)}\\
\frac{d\delta S_p^y}{dt} &= -\frac{2JS}{\hbar}(2\delta S_p^x - \delta S_{p-1}^x - \delta S_{p+1}^x), && \text{(A.10)}\\
\frac{dS_p^z}{dt} &= 0. && \text{(A.11)}
\end{aligned}$$

Now, we have two coupled differential equations and look for plane wave solutions of the form:

$$\begin{aligned}
\delta S_p^x &= u e^{i\mathbf{k}\cdot\mathbf{r} - i\omega t}, && \text{(A.12)}\\
\delta S_p^y &= v e^{i\mathbf{k}\cdot\mathbf{r} - i\omega t}, && \text{(A.13)}
\end{aligned}$$

where we can let $\mathbf{k}\cdot\mathbf{r} = pqa$ by introducing a spacing a between spins, and ascribing a magnitude of q to the spin wave's wave vector, $\mathbf{k}$. If we take the derivative of eq. (A.12) and put this equal to eq. (A.9), we find that:

$$-i\omega tu = \frac{2JS}{\hbar}(v(2 - (\mathrm{e}^{-iqa} + \mathrm{e}^{iqa}))) \tag{A.14}$$

$$= \frac{4JSv}{\hbar}(1 - \cos(qa)). \tag{A.15}$$

Doing a similar calculation for the other equation, one finds $u = iv$ yielding the dispersion relation

$$\hbar\omega = 4JS(1 - \cos(qa)). \tag{A.16}$$

Appendix B $J_{1-5}D$ model for GGG

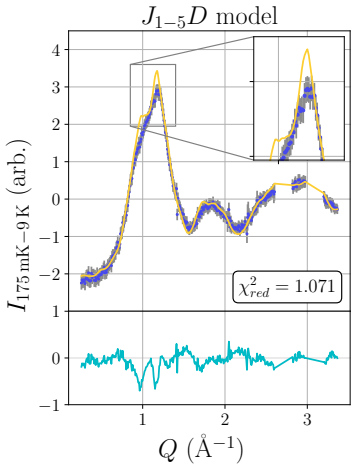

Figure 22: Addition to fig. 7 for a model that also includes the J_5 parameter.

$Gd_3Ga_5O_{12}$	J_1(mK)	J_2(mK)	J_3(mK)	J_4(mK)	J_5(mK)	$\mathcal{D}$ (mK)
Fit $J_{1-5}D$	127 ± 3	-7 ± 1	4.8 ± 0.7	1 ± 1	3 ± 1	45.7*

Table 4: Fitted parameters for GGG with a $J_{1-5}D$ model. * indicates a fixed parameter.

Appendix C GGG $J_{1-4}\mathcal{D}$ fit with 66% more BZ-points

$Gd_3Ga_5O_{12}$	J_1(mK)	J_2(mK)	J_3(mK)	J_4(mK)	$\mathcal{D}$ (mK)
Fit $J_{1-4}D$	129 ± 2	-3.85 ± 0.09	4.3 ± 0.6	4.0 ± 0.4	45.7*

Table 5: Fitted parameters for GGG with a $J_{1-4}\mathcal{D}$ model and 66% more BZ-points. * indicates a fixed parameter.

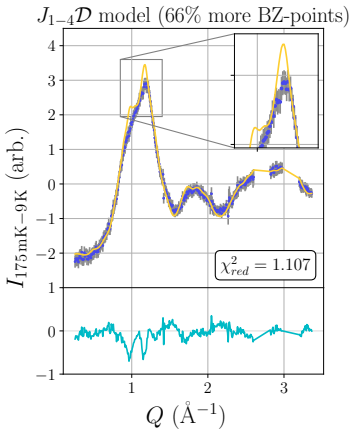

Figure 23: A $J_{1-4}\mathcal{D}$ fit for GGG $T = 0.175\,\text{K}$. 66% more BZ-points used than the fits in fig. 7

Appendix D YbGG full fits

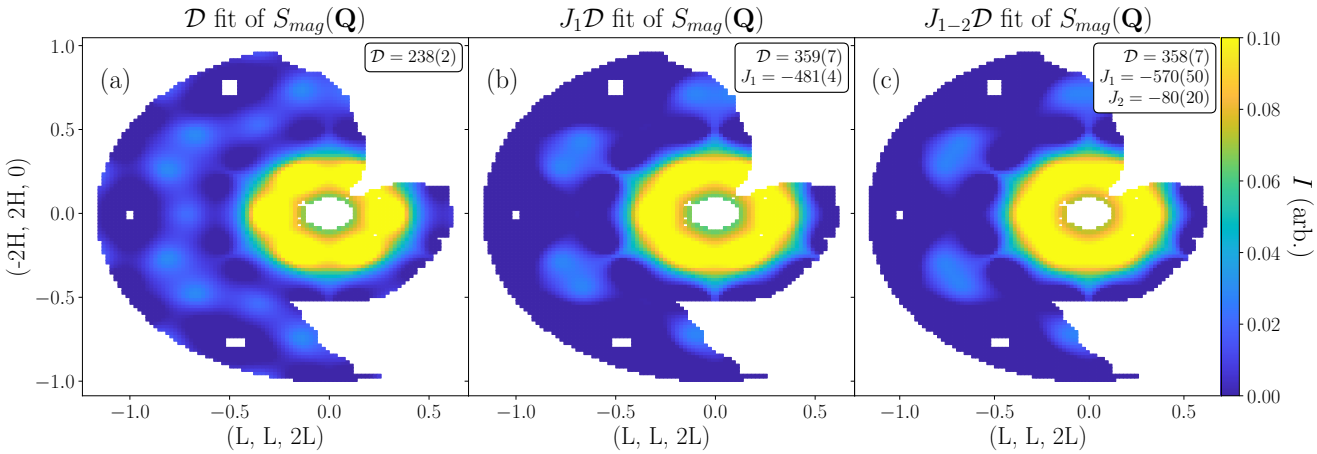

Figure 24: Same fits as shown in fig. 14 but without $S_{mag}(\mathbf{Q})$. (a) $\mathcal{D}$ fit, (b) $J_1\mathcal{D}$ fit, and (c) $J_{1-2}\mathcal{D}$ fit. Incident energy of $E = 1.55\,\text{meV}$. Numbers in top right boxes show fitted interaction parameters and have units of mK. Number in parentheses indicate ± uncertainty.

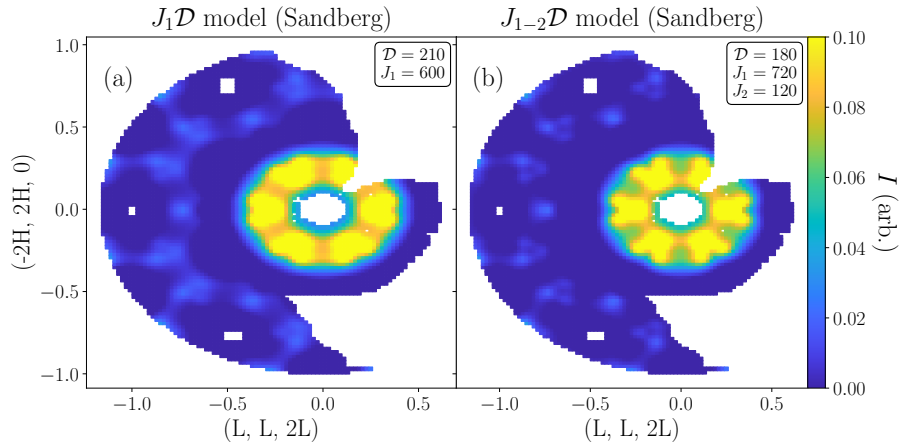

Figure 25: Models from [11] calculated with Spinteract. (a) $J_1\mathcal{D}$ model and (b) $J_{1-2}\mathcal{D}$ model. Incident energy of $E = 1.55\,\text{meV}$.

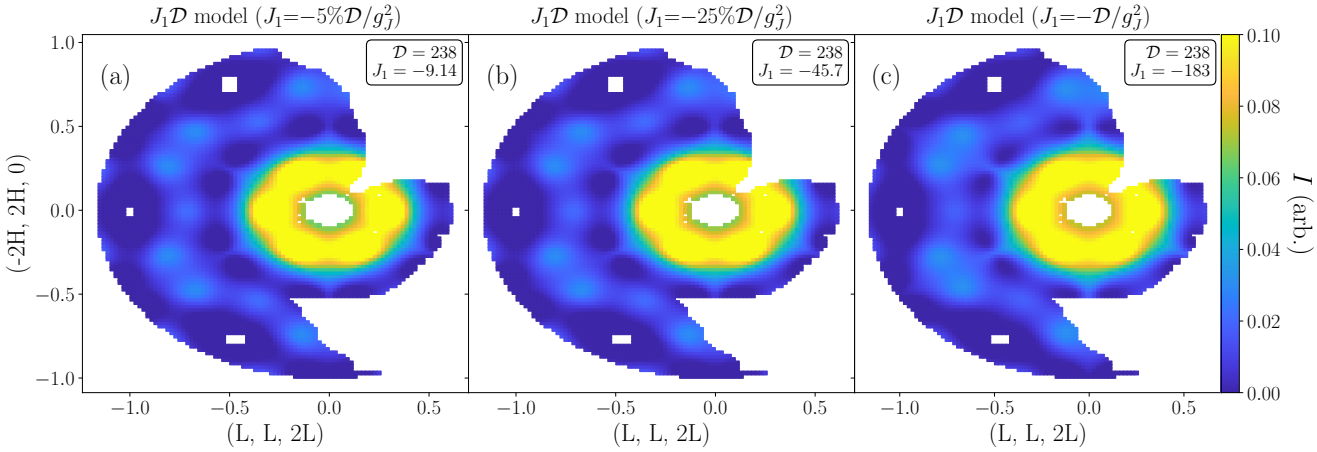

Figure 26: $J_1\mathcal{D}$ models calculated with Spinteract for varying J_1. (a) $J_1 = -5\%\mathcal{D}/g_J^2$, (b) $J_1 = -25\%\mathcal{D}/g_J^2$, and (c) $J_1 = -\mathcal{D}/g_J^2$. Incident energy of $E = 1.55\,\text{meV}$.

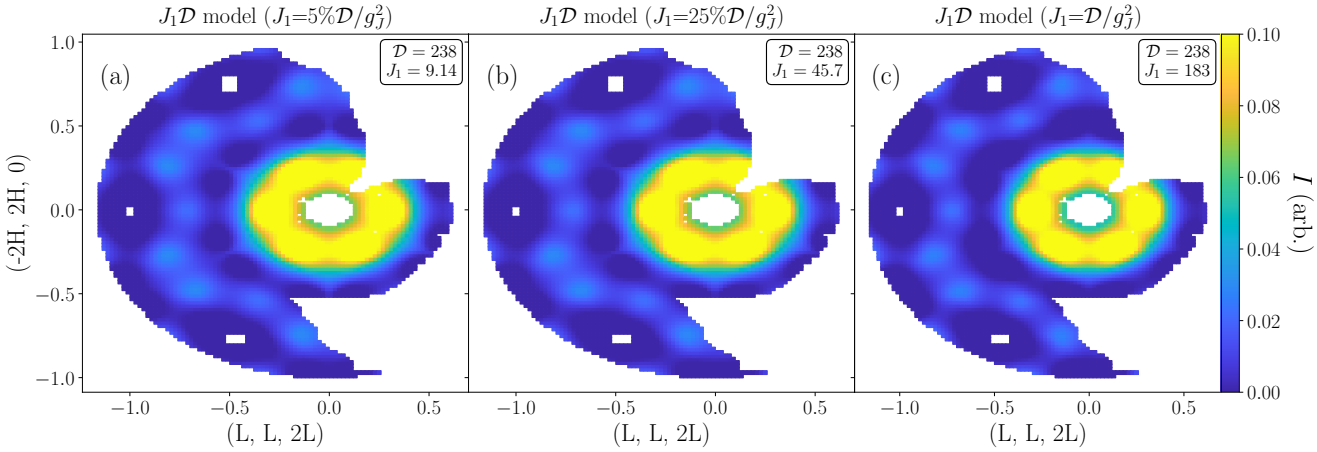

Figure 27: $J_1\mathcal{D}$ models calculated with Spinteract for varying J_1. (a) $J_1 = 5\%\mathcal{D}/g_J^2$, (b) $J_1 = 25\%\mathcal{D}/g_J^2$, and (c) $J_1 = \mathcal{D}/g_J^2$. Incident energy of $E = 1.55\,\text{meV}$.

Appendix E YbGG $J_1\mathcal{D}$ model $J_1 = \pm 2\mathcal{D}/g_J^2$.

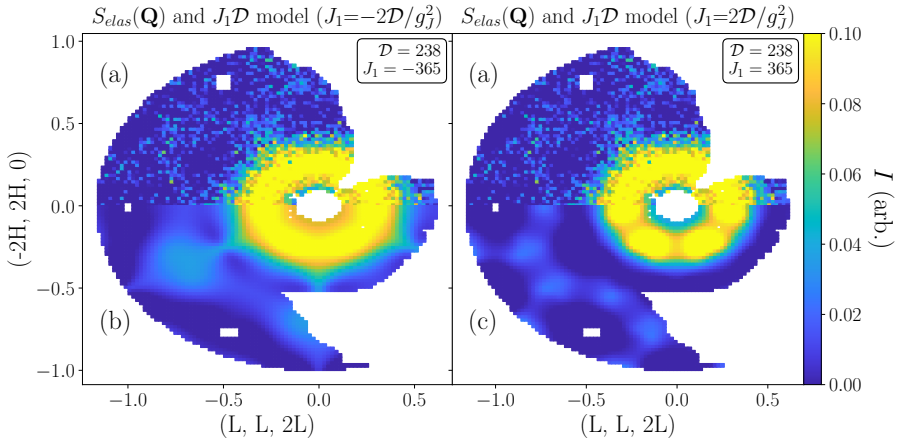

Figure 28: (a) $S_{elas}(\mathbf{Q})$. $J_1\mathcal{D}$ models calculated with Spinteract for varying J_1 with (b) $J_1 = -2\mathcal{D}/g_J^2$, and (c) $J_1 = 2\mathcal{D}/g_J^2$. Incident energy of $E = 1.55$ meV.

Appendix F YbGG more fits/models ($E = 3.32$ meV)

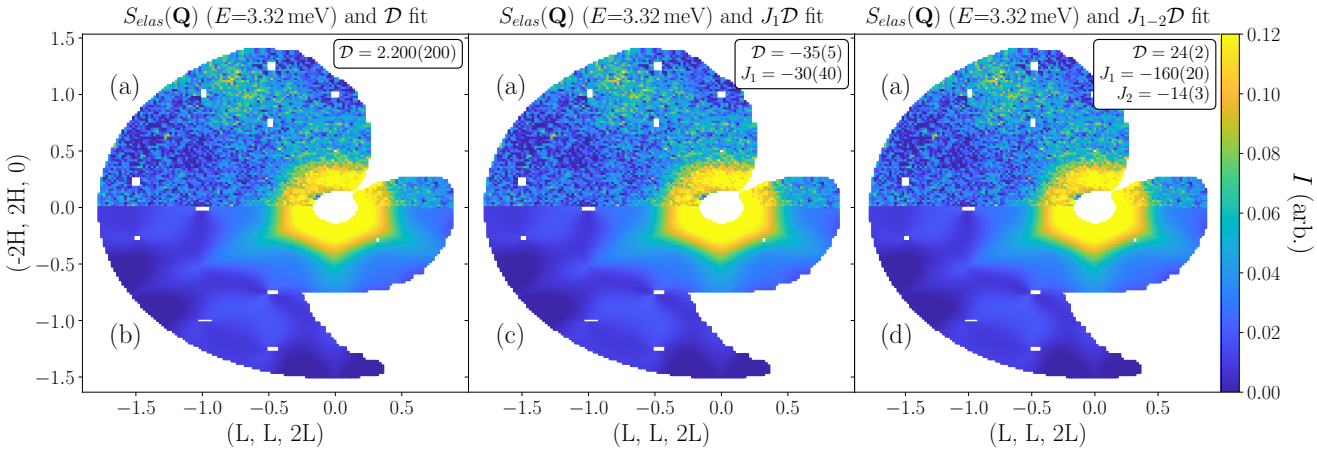

Figure 29: (a) $S_{elas}(\mathbf{Q})$ ($E = 3.32$ meV). Spinteract fits with (b) $\mathcal{D}$ fit, (c) $J_1\mathcal{D}$ fit, and (d) $J_{1-2}\mathcal{D}$ fit. Incident energy of $E = 3.32$ meV. Numbers in top right boxes show fitted interaction parameters and have units of mK. Number in parentheses indicate ± uncertainty.